DYNAMICS OF THE HOMOTRIMERIC TOLC TRANSMEMBRANE PROTEIN

by

IŞIK KANTARCIOĞLU MAZMANOĞLU

Submitted to the Graduate School of Engineering and Natural Sciences

in partial fulfillment of

the requirements for the degree of

Doctor of Philosophy

Sabancı University

June 2024

DYNAMICS OF THE HOMOTRIMERIC TOLC TRANSMEMBRANE PROTEIN

APPROVED BY:

Prof. Dr. Canan Atılgan ....Canan Atılgan....
(Thesis Supervisor)

Prof. Dr. Ali Rana Atılgan ....Ali Rana Atılgan....

Asst. Prof. Dr. Nur Mustafaoğlu ....

Prof. Dr. Özlem Keskin ....

Assoc. Prof. Dr. Özge Şensoy ....

DATE OF APPROVAL: 28/06/2024

© Işık Kantarcıoğlu Mazmanoğlu 2024

ALL RIGHTS RESERVED

ABSTRACT

DYNAMICS OF THE HOMOTRIMERIC TOLC TRANSMEMBRANE PROTEIN

Işık Kantarcıoğlu Mazmanoğlu

Molecular Biology, Genetics and Bioengineering, Ph.D. Thesis, 2024

Thesis Supervisor: Canan Atılgan

Keywords: Antibiotic efflux, multidrug resistance, protein structural dynamics, drug design, evolutionary trade-offs, saturation deep mutagenesis

Efflux-mediated β-lactam resistance poses a significant challenge to public health, undermining the effectiveness of various β-lactam antibiotics against a multitude of clinically relevant pathogenic bacteria. Structural and functional analyses have elucidated the role of the efflux protein TolC in several Gram-negative bacteria as a conduit for antibiotics, bacteriocins, and phages, impacting bacterial susceptibility and virulence. This study undertook a comprehensive examination of β-lactam drug efflux mediated by TolC, employing extensive experimental and computational analyses. Our computational investigations delved into the molecular dynamics of drug-free TolC, revealing critical unidirectional movements of the trimeric TolC and identifying residues significantly involved in TolC opening. To validate these findings, a whole-gene-saturation mutagenesis assay was conducted, systematically mutating each residue of TolC to 19 other amino acids and assessing the fitness effects of these mutations under β-lactam-induced selection. Oxacillin, piperacillin, and carbenicillin were selected for study due to their varying efficiencies in being effluxed by the AcrAB-TolC complex. This approach elucidated similarities and differences in the efflux processes of the three β-lactam antibiotics through trimeric TolC. Further analysis via steered molecular dynamics simulations unveiled general and drug-specific efflux mechanisms employed by TolC. Key positions at the periplasmic entry of TolC were identified, whose altered dynamics influence long-range efflux motions as allosteric modulators. These findings offer valuable insights into the structural dynamics of TolC, laying a foundation for understanding multidrug resistance mechanisms and informing the design of novel antibiotics capable of circumventing bacterial efflux mechanisms

ÖZET

HOMOTRİMERİK TOLC TRANSMEMBRAN PROTEİNİNİN DİNAMİĞİ

Işık Kantarcıoğlu Mazmanoğlu

Moleküler Biyoloji, Genetik ve Biyomühendislik, Doktora Tezi, 2024

Tez Danışmanı: Canan Atılgan

Anahtar kelimeler: Antibiyotiklerin hücre dışına atılması, çoklu ilaç direnci, yapısal protein dinamikleri, evrimsel değişimler, derin mutasyon taraması

Dışa atım aracılı β-laktam direnci, çeşitli β-laktam antibiyotiklerinin klinik çalışmalarda patojenik bakterilere karşı antibiyotik etkinliğini zayıflatarak halk sağlığını tehlikeye atmaktadır. Yapısal ve işlevsel analizler, Gram-negatif bakterilerde TolC proteininin antibiyotikler, bakteriyosinler ve fajlar için bir kanal olarak kullanıldığını, bakterinin duyarlılığı ve virülansı üzerindeki rolünü aydınlatmıştır. Bu çalışma, deneysel ve hesaplamalı analizleri kullanarak TolC'nin aracılık ettiği β-laktam ilaç akışının kapsamlı bir incelemesidir. Hesaplamalı araştırmalarımız, ilaç içermeyen TolC proteininin moleküler dinamik benzetimlerini inceleyerek TolC'nin tek yönlü hareketlerini ortaya çıkarmış ve TolC'nin açılmasında önemli rol oynayan amino asitleri belirlemiştir. Bu bulguları doğrulamak için, TolC'nin her bir amino asidini sistematik olarak 19 diğer amino aside mutasyona uğratan ve bu mutasyonların β-laktam kaynaklı seçilim altındaki uygunluk etkilerini değerlendiren tüm gen saturasyon mutajenez deneyleri gerçekleştirildi. Oksasilin, piperasilin ve karbenisilin antibiyotik molekülleri AcrAB-TolC kompleksi tarafından dışa atılırken farklı verimliliklerde olmaları sebebiyle seçildi. Bu çalışma, üç β-laktam antibiyotiğinin TolC aracılığıyla dışa atılma süreçlerindeki benzerlik ve farklılıkları ortaya çıkarmıştır. Yönlendirilmiş moleküler dinamik simülasyonları yoluyla yapılan analizler, TolC tarafından kullanılan genel ve ilaca özgü dışarı atma mekanizmalarını ortaya çıkarmıştır. TolC'nin periplazmik girişinde, değişim durumunda allosterik düzenleyici olarak dışa atma hareketini protein boyunca etkileyen kilit pozisyonlar tanımlanmıştır.

Bu bulgular, TolC'nin yapısal dinamikleri hakkında değerli bilgiler sunarak çoklu ilaç direnci mekanizmalarını anlamak ve bakteriyel dışa atma mekanizmalarından kaçabilen yeni antibiyotiklerin tasarlanmasına bir temel oluşturmaktadır.

To my family.

ACKNOWLEDGEMENTS

In my Ph.D. education, I am grateful for the countless learning moments and the truly remarkable individuals who have crossed my path. Their guidance and support enriched my experience beyond measure. There are so many people to whom I owe my appreciation. I would like to start by expressing my gratitude to my advisor, Dr. Canan Atılgan. Her endless patience, enthusiasm for sharing her knowledge, and guidance brought this thesis to life. I also want to thank Dr. Ali Rana Atılgan for his support and guidance. His passion for science acted as a propelling force that kept me motivated in my research.

Next, I want to thank my jury members, Drs. Özge Şensoy, Özlem Keskin, and Nur Mustafaoğlu for their interest and valuable feedback. I want to express my sincere gratitude to Dr. Mert Gür for his contributions and discussions along my dissertation progress meetings. Additionally, I extend my thanks to Dr. Canan Atılgan and Dr. Ali Rana Atılgan once again for providing us with a stable research environment. As a part of this stable research environment, I would like to thank all the former and current members of the MIDST Lab for their cooperation. We overcame graduate school paperwork obstacles and shared many mind-opening discussions over countless cups of coffee with Büşra Tayhan, Erhan Ekmen, Dr. Ebru Çetin, Dr. Gökşin Liu, Kurt Arıcanlı, Melike Berksöz, and Dr. Tandaç Fürkan Güçlü. I want to specifically thank Dr. Tandaç Fürkan Güçlü for sharing his knowledge, friendship, and coffee breaks during this journey with me. His unexpected, funny sounds and text messages not only made me laugh but also served as notifications of interesting scientific progress he had read about.

I am grateful for the year I spent in the USA. It not only helped me gain a scientific perspective and wet-lab experience but also provided me priceless life experiences. I want to thank Dr. Erdal Toprak for his mentorship and the opportunity he provided. I also want to thank my lab mates in the Toprak Lab: Adam Lyon, Ayesha Ahmed, Ilona K. Gaszek, Dr. Marinelle Rodrigues, and Dr. M. Sadık Yıldız, who supported me in the lab and social life. I had a great time working in the lab with them. Here, I want to thank Ilona and her dear family separately. I am grateful to her for sharing her time, knowledge, and friendship with me.

Last but not least, my father Mehmet always believed in me, my mother Sevilay was a constant reminder to get up and do my best, and my brother Ege was a unique ally, source of

motivation, and humor for me. My beloved one, Onur, kept me together and convinced me to believe in myself throughout this journey. I continuously felt their unconditional support, for which I am deeply grateful.

In short, I would like to thank everyone whose names I have mentioned or not mentioned, who reminded me that I never walk alone.

The numerical calculations reported in this thesis were performed at TUBITAK ULAKBIM, High Performance and Grid Computing Center (TRUBA resources), Sabancı University's HPC clusters and BioHPC at University of Texas Southwestern Medical Center. This thesis was funded by the TÜBİTAK 122F149 project and partially funded by BIDEB 2214-A scholarship program.

TABLE OF CONTENTS

LIST OF FIGURES

LIST OF TABLES

LIST OF ABBREVIATIONS

°C	Celsius degrees
Å	Ångström
β	Inverse thermal energy
C_α	Alpha carbon
$\mathbf{C}$	Variance-Covariance Matrix
CBC	Carbenicillin
CFU	Colony Forming Unit
CGSC No.	Coli Genetic Stock Center Number
Cl	Chlorine
DMS	Deep Mutational Scanning
FEP	Free Energy Perturbation
fs	femtosecond
K	Potassium or Kelvin
k_B	Boltzmann Constant
kcal	kilocalorie
LJP	Lennard-Jones Potential
MD	Molecular Dynamics
MIC	Minimum Inhibitory Concentration
MuMi	Mutation Minimization
μg	microgram
μl	microliter
μs	microsecond

Na	Sodium
NMA	Normal Mode Analysis
ns	nanosecond
OD600	Optical density at a wavelength of 600 nanometer in 1-centimeter light path
OEP	Outer Membrane Protein
OMF	Outer Membrane Factor
OXA	Oxacillin
PC	Principal Components
PCA	Principal Component Analysis
PDB	Protein Data Bank
PRS	Perturbation Response Scanning
ps	picosecond
POPE	1-Palmitoyl-2-oleoyl-sn-glycero-3-phosphoethanolamine
PIP	Piperacillin
RMSD	Root-Mean Square Deviation
RMSF	Root-Mean Square Fluctuation
RND	Resistance-Nodulation Division
RPM	Rotation per minute
σ	Standard Deviation
SEM	Standard error of the mean
SMD	Steered Molecular Dynamics
SML	Saturation Mutagenesis Library
T	Temperature

TCA	Triangular Cross-sectional Area
UT	Untreated
WHO	World Health Organization
WT	Wild-Type

1. INTRODUCTION

1.1 Antimicrobial Resistance

The statistical data from 2019 estimated that around 1.27 million fatalities worldwide were attributed to bacteria resistant to antibiotics, with an additional five million deaths linked to these resistant strains.[1] World Health Organization (WHO) classified pathogens according to the urgency of needed antibiotics. The top six pathogens linked to deaths due to antibiotic resistance, *Escherichia coli, Staphylococcus aureus, Klebsiella pneumoniae, Streptococcus pneumoniae, Acinetobacter baumannii, and Pseudomonas aeruginosa*, were identified as priority pathogens by WHO. Almost all of these priority pathogens are Gram-negative bacteria.[2]

Gram-negative bacteria employ various strategies to evade the impacts of antibiotic molecules, including adaptive, acquired, and intrinsic forms of resistance.[3] Adaptive resistance is defined as the modulation of gene expression in response to environmental signals like stress, pH changes, or exposure to sub-inhibitory doses of antibiotics. In adaptive resistance, bacteria rapidly adapt to antibiotic exposure. Once the resistance triggering signal diminishes from the environment, bacteria usually return to their original susceptibility state.[4] Acquired resistance arises when bacteria obtain resistance genes from the extracellular sources (horizontal gene transfer) by transformation, transduction or conjugation.[5–7] Intrinsic resistance is when bacteria naturally have ways to resist antibiotics, like limiting drug uptake, altering the antibiotic targeted sites, inactivating drugs, or pumping antibiotics out of the bacteria (active drug efflux). Most of the intrinsic resistance mechanisms in Gram-negative bacteria often involve efflux pumps belonging to the resistance-nodulation division (RND) family, which play a significant role in conferring clinically relevant levels of antimicrobial resistance.[8–10]

1.2 TolC: An outer membrane protein with a critical role in antibiotic efflux

Gram-negative bacteria have evolved transport mechanisms to move macromolecules and toxic compounds across membranes.[11] These mechanisms play important roles in drug resistance to current and future antibiotics.[12] Bacterial efflux is one of the primary systems responsible for the emergence of multidrug resistance since efflux machineries in bacteria can pump out several different types of antibiotics with varying rates and specificity.[13,14] The RND family is one of the major efflux pump superfamilies in Gram-negative bacteria. These pumps consist of a transporter protein located in the inner membrane of the bacterium; an adaptor protein, also referred to as a membrane-fusion protein, found in the periplasmic space; and an outer membrane protein. Efflux pumps organized as tripartite complexes have the capability to efflux a broad range of substances, including clinically important antibiotics such as β-lactams, bile salts, and detergents.[15,16] Efflux via RND-family pumps is powered by the proton motive force, where the movement of hydrogen ions drives transport of the substrate.[17]

The major multidrug-resistant efflux pump that is a member of the RND family in *Escherichia coli* (*E. coli*) is the AcrAB-TolC protein complex.[17] In Gram-negative bacteria, the outer membrane protein TolC can transiently associate with the protein pairs AcrAB, MacAB, and EmrAB to create various tripartite efflux pump assemblies as a response to elevated antibiotic concentrations inside bacteria (Figure 1.1).[18] These efflux assemblies, which span the length of the periplasmic space, expel toxic substances from the cytoplasm to the extracellular region. Understanding specificity of the efflux pumps towards various substrates will lead to drug development strategies to avoid or inhibit them.[19]

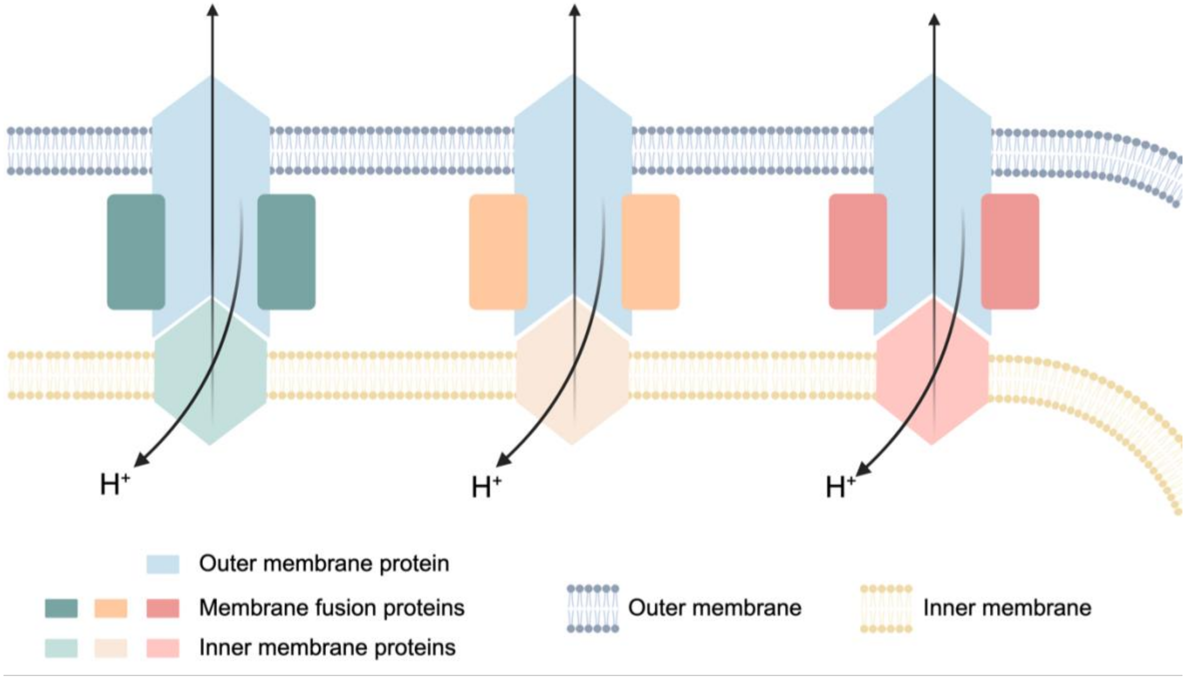

Figure 1.1 Efflux protein complexes. Outer membrane proteins can make various efflux systems by interacting with membrane fusion proteins and inner membrane proteins to efflux different types of molecules.

TolC is a multifunctional protein that is subject to conflicting evolutionary selection pressures. While TolC is crucial to protect bacterial cells against antibiotics and other antibacterial compounds, its presence can impose a risk for bacterial cells, since TolC can also function as a portal for the transport of bacteriocins and bacteriophages into the cells (Figure 1.2A).[20–23] Thus, bacteria need to strike an evolutionary balance between making TolC available when efflux is necessary and limiting it as an entry point when efflux presents risk.[24]

Previous structural studies reveal that TolC functions as a homotrimer, consisting of 22 amino-acid-long signaling part and 493 amino-acid-long mature TolC protein for each protomer. 43 residues at the carboxy terminal were removed to obtain crystal structure. Its 12-stranded β-barrel part is embedded into the outer membrane and is approximately 40 Å long; its cone-like α-helical coiled-coil domain extends into the periplasm (Figure 1.2B) spanning an additional 100 Å.[25] The outer membrane channel opening, especially the periplasmic end opening, is necessary to initiate the process of the expulsion of the antibiotic molecules.[26] The crystallized TolC structure of the closed form consists of 428 amino acids in each protomer.[25] These protomers assemble into the homo-trimeric TolC structure.

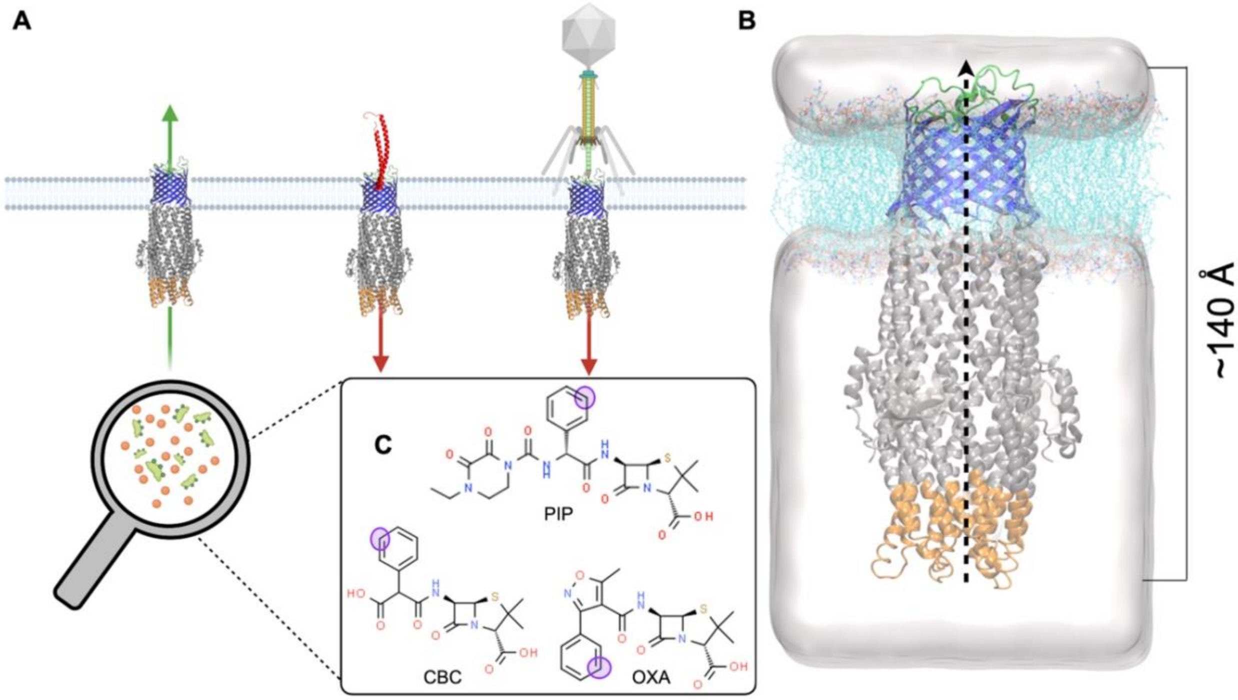

Figure 1.2 | TolC and ligand structures. (A) TolC structure positioned in outer membrane. The major known role of TolC in *E. coli* is to expel antibiotics and bile salts to the outside of the cell which is essential for bacterial survival (green arrow). However, it is also an entry point for colicin-E1 (partial structure shown in red) and some bacteriophages which results in cell death (red arrows). (B) TolC embedded in a POPE lipid membrane (cyan) and placed in a simulation box shown as a white blob; extracellular loops are colored in green, membrane embedded β-barrel is colored in blue, α-helices extended through periplasmic space are colored in gray and the approximately 30 Å part located at the periplasmic tips of the protein is colored in orange. This coloring scheme is maintained throughout the thesis. The reaction coordinate of the drug is defined from the entry point to the exit and spans ~140 Å (dashed line). (C) Two-dimensional representations of the antibiotics studied in this work. Carbenicillin (CBC), piperacillin (PIP), and oxacillin (OXA); SMD pulling atoms for the drug molecules are shown as purple circles.

We note that TolC's role in antibiotic efflux is highly dependent on its interactions in the resulting AcrAB-TolC complex. The conformational state of AcrB has been proposed to be transmitted to TolC by AcrA, leading to the opening of TolC.[27] Mutations in the periplasmic tip of TolC have been shown to change this communication within the AcrAB-TolC complex[26,28,29] Bavro *et al.* investigated the importance of a network of hydrogen bonds and salt bridges involving Y362 and

R367 to maintain the closed state of TolC. Y362F/R367E double mutants disrupted this network which resulted in increased sensitivity to vancomycin.[26] Pei *et al*. proposed the importance of T152, D153, Y362, and R367 to constrain efflux. R367S mutation increased the channel's conductance up to four-fold and the Y362F/R367S double mutation by nearly 15-fold. It has been proposed that the destabilization of ionic and hydrogen bonds at the periplasmic tip could dilate the TolC pore entrance and allow substrate passage.[28] D371V is another highlighted mutation which has notable impact on growth even without the presence of antibiotics, leading to increased susceptibility to the tested substrates. The study identified antibiotic-specific phenotypes linked to novel mutations in TolC, indicating that substrate specificity may not be exclusively determined by the transporter protein or the periplasmic adaptor protein (PAP). Instead, it suggests that the TolC channel itself may play a significant role in determining substrate specificity.[29] Nevertheless, the role of TolC-drug interactions on the rate of efflux and TolC's contributions to the selectivity once the drug has been delivered to its channel have not been interrogated.

1.3 Important structural regions and rearrangements in TolC and its homologs

TolC is a member of outer membrane efflux protein (OEP) family (or "Outer Membrane Factor (OMF)" family) which are involved in the efflux mechanism of transport of small molecules and toxins across the outer membrane of Gram-negative bacteria.

Outer membrane protein OprM from *Pseudomonas aeruginosa* is one of the closest homologs of *E. coli* TolC. Normal mode analysis (NMA) based on elastic network models[30] was previously used to uncover the conformational states of OprM and how they compare to the open state of TolC.[31] In the closed form of TolC, coiled-coil helices linked by salt bridges and hydrogen bonds at the tip of the periplasmic entrance provide selectivity and constrictions for substance transport, particularly maintained by D371 and D374.[26,28] CmeC found in *Campylobacter jejuni* is another homologue that shares structural similarities with TolC. Substrate efflux mechanisms with CmeC have also been simulated by others[32] using steered molecular dynamics (SMD) simulations.[33] Their results indicated the anionic bile acid moves up the channel by climbing a ladder of acidic residues that align in the interior surface of the protein. Unlike CmeC, TolC has far fewer charged residues along the efflux path, which indicates a different mechanism of action.

These findings and the critical importance of TolC in antibiotic resistance motivate our exploration of the structural shifts in the TolC protein at the atomistic level. We first utilized molecular dynamics (MD) simulations for both the closed and the open forms of drug-free TolC to determine its intrinsic dynamics and structural transitions that are difficult to observe by most experimental methods. Principal component analysis[34,35] of MD trajectories suggested that TolC has an intrinsic expelling movement in both closed and open forms. The dominant modes of these forms displayed net movement in the direction of efflux and, hence, suggest these motions may play an important role in expelling antibiotic molecules. Since TolC conformations can switch between closed and open forms, we hypothesized that there must be important residues whose perturbation might tip the equilibrium between the two conformations.

To systematically search for these residues, we utilized the perturbation response scanning (PRS) that we previously developed as a robust and now a widely used method for identifying essential residues that trigger conformational changes of proteins.[36,37] PRS relies on linear response theory to determine specific residues that, when perturbed via external forces, might lead to conformational changes in proteins. PRS has been successfully used by several groups to identify structurally important regions not only in many monomeric proteins but also in multimeric assemblies such as HSP90.[38] PRS also was applied to unravel motions that trigger uncoating when applied to a multiprotein capsid comprised of 60 protomeric units, each of which contained four heterogenic subunits.[39]

1.4 Exploring Dynamical Shifts within the TolC Structure Enabling the Efflux of Three β-Lactam Antibiotics: Carbenicillin, Piperacillin, and Oxacillin

The choice of β-lactam antibiotics in this thesis was due to their great importance in fighting against bacterial infections and the rapid evolution of β-lactam resistance in clinical and community settings. Almost 80 percent of all antibiotics used in clinics are β-lactams. Although resistance to β-lactams is often attributed to the spread of β-lactamase genes producing β-lactamases that render β-lactams ineffective by hydrolyzing them, many β-lactam antibiotics are ineffective against Gram-negative bacteria because of their fast efflux from the cytoplasm. For instance, it was previously shown that disruption of the AcrAB-TolC complex in *E. coli* can reduce the required dose of oxacillin to kill bacterial cells by almost three orders of magnitude.[23] We chose oxacillin, piperacillin, and carbenicillin for our study due to the distinct efflux efficiencies of the AcrAB-TolC complex towards these antibiotics—high for oxacillin, moderate for piperacillin, and low for carbenicillin. To substantiate these efficiencies, we compared the minimum inhibitory concentrations (MICs) needed to inhibit a wild-type *E. coli* strain, a *tolC*-deficient mutant, and the mutant harboring a *tolC*-carrying rescue plasmid.

We also systematically explored the fitness effects of single amino acid replacements at each position in TolC using a saturation mutagenesis library under selection with each of these drugs. Finally, we utilized SMD simulations to calculate work curves during passage of these drug molecules through TolC homotrimer opening to determine drug specific and generalist TolC residues involved in β-lactam efflux.

2. MATERIALS AND METHODS

2.1 Molecular Dynamics Simulations

The average protein conformation observed in crystal structures often does not accurately represent its natural structure. MD simulations, which use statistical mechanics to track how atoms move over time, recreate the protein’s natural environment, including solvent, temperature, and pressure.

Physical movements of atoms and molecules are predicted over time by solving Newton's equation of motion (**F** = m**a**). The force **F** acting on each particle is derived from the potential energy function $U(r)$, which depends on the positions r of all particles.

$$\mathbf{F} = -\nabla U(r) \tag{2.1}$$

Potential energy function is built on the summation of the bonded and nonbonded interactions.

Bonded interactions are covalent bonds, bond angles, and torsion angles.

- **Covalent bonds:** Modeled using a harmonic potential:

$$U_{bond}(r) = \frac{1}{2}k_b(r - r_0)^2 \tag{2.2}$$

where r is the bond length, r_0 is the equilibrium bond length, and k_b is the bond force constant.

- **Bond angles:** Also modeled with a harmonic potential:

$$U_{angle}(\theta) = \frac{1}{2}k_\theta(\theta - \theta_0)^2 \tag{2.3}$$

where θ is the bond angle, θ_0 is the equilibrium angle, and k_θ is the angle force constant.

- **Torsion angles:** Modeled with a periodic potential:

$$U_{torsion}(\phi) = \sum_n \frac{1}{2}V_n[1 + \cos(n\phi - \gamma)] \tag{2.4}$$

where ϕ is the dihedral angle, V_n is the amplitude, n is the periodicity, and γ is the phase offset.

Non-bonded interactions utilize the Lennard-Jones (LJ) Potential to model van der Waals forces and the Coulomb potential to model electrostatic interactions.

- **Lennard-Jones Potential** models van der Waals forces:

$$U_{\mathrm{LJ}}(r) = 4\epsilon\left[\left(\frac{\sigma}{r}\right)^{12} - \left(\frac{\sigma}{r}\right)^{6}\right] \tag{2.5}$$

where r is the distance between two atoms, ϵ is the depth of the potential well, and σ is the finite distance at which the inter-particle potential is zero.

- **Coulomb Potential** models electrostatic interactions:

$$U_{\mathrm{Coulomb}}(r) = \frac{q_1 q_2}{4\pi\epsilon_0 r} \tag{2.6}$$

where q_1 and q_2 are the (partial)charges of the interacting particles, ϵ_0 is the vacuum permittivity, and r is the distance between charges.

The total potential energy $U(\mathrm{r})$ is the sum of these contributions:

$$U(r) = U_{bond} + U_{angle} + U_{torsion} + U_{\mathrm{LJ}} + U_{\mathrm{Coulomb}} \tag{2.7}$$

This combined potential energy function governs the forces acting on each particle, which are derived as $\mathbf{F} = -\nabla U(r)$, and these forces are then used to update the positions and velocities of the particles over time.

By integrating these forces over time, using algorithms like the Verlet or Velocity-Verlet integrator, particle velocities and positions are updated. In MD simulations, all energy terms are parametrized in force fields. To resolve the equations of motion, it is sufficient to provide the initial spatial coordinates for all atoms in the system, as the initial velocities are randomly assigned according to Maxwell-Boltzmann distribution corresponding to the given temperature.[40]

The closed state x-ray structure (PDB ID: 1EK9)[25], and open state cryo-electron microscopy (cryo-EM) structure (PDB ID: 5NG5)[27] were used as the initial TolC coordinates for MD simulations. The D371G mutant which we hypothesized destroyed key salt bridges on the periplasmic entrance side of TolC was also investigated via MD simulations; the initial coordinates of this mutant were created using Pymol.[41] These coordinates were subjected to MD simulations to understand the time dependent behavior of the protein under physiological conditions. Since TolC is a Gram-negative bacterium protein spanning the outer membrane and the periplasmic space, the orientation of TolC was arranged with the Orientations of Proteins in Membranes (OPM) database.[42,43] The overall system was prepared on the CHARMM-GUI platform.[44–47] The protein of interest was embedded with in a phospholipid bilayer comprising 256 molecules of 1-Palmitoyl-2-oleoyl-sn-glycero-3-phosphoethanolamine (POPE), distributed across both the upper and lower leaflets with a balanced ratio of 128 lipids per leaflet. To mimic the natural isotonic environment, the system was solvated using the TIP3P water model[48], ensuring a realistic representation of solvent behavior. Furthermore, to replicate the ionic composition of physiological conditions, sodium (Na^+) and chloride (Cl^-) ions were introduced into the system, achieving the isotonic conditions of 0.15 M.

We also carried out nine ‘free MD simulations’ by placing carbenicillin molecule in closed x-ray structure at different locations along the channel. In three of these simulations, carbenicillin molecule was located at the periplasmic entry side which corresponds 0-25 Å region of the protein (see Fig 1B), three are in the central region where the transfer of the drug molecules to the exit region occurs (25-100 Å), and the other three are in the exit region (100-140 Å).

MD simulations were performed using NAMD[49,50] and CHARMM36 force field parameters with periodic boundary conditions.[45] The total number of atoms for all our simulations are ca. 150,000 with box dimensions of 94 × 94 × 173 Å. The particle-mesh Ewald method with a grid spacing of maximal 1 Å per grid in each dimension was used.[51] 12 Å cutoff radius with a switching function turned on at 10 Å was applied to calculate van der Waals interactions. The RATTLE algorithm[52] was utilized to set the step size of 2 fs during numerical integration with the Verlet algorithm. Temperature regulation was managed with the Langevin thermostat using a damping coefficient of

5 ps^{-1}. Pressure regulation was achieved through a Nose-Hoover Langevin piston, and volume variations were set to remain uniform in all directions. Systems were minimized for 50,000 steps to remove undesired van der Waals contacts. The energy-minimized systems were subjected to 5 ns MD run with constant temperature control (NVT). The production parts of the MD simulations of length 500 ns were run in the isothermal-isobaric (NPT) ensemble at 310 K and 1 atm.

2.2 Trajectory Analyses

Root-mean square deviation (RMSD) and root-mean square fluctuation (RMSF) are two of the basic MD simulation analyses. The RMSD is used to measure the deviation of the properly aligned atom positions from a reference structure to provide insights into structural stability and conformational changes of the molecule. The reference structure is the initial (PDB) structure in our case. The formula for RMSD between two sets of C_α atomic coordinates r (reference) and r' (target) is:

$$\text{RMSD} = \sqrt{\frac{1}{N}\sum_{i=1}^{N}(r_i - r'_i)^2} \tag{2.8}$$

where N is the number of C_α atoms, r_i is the position vector of the i^{th} atom in the reference structure, r'_i is the position vector of the i^{th} C_α atom in the structure.

The RMSF is a measure used to quantify the flexibility of atoms in MD simulations. For each time frame, the deviation of each C_α atom from the reference position is computed. The formula for RMSF for i^{th} C_α atom in the structure is given by:

$$\text{RMSF}_i = \sqrt{\frac{1}{T}\sum_{t=1}^{T}(r_i(t) - \bar{r}_i)^2} \tag{2.9}$$

where T is the number of frames in simulation, $r_i(t)$ is the position vector of i-th C$_\alpha$ atom at time t, $\bar{r}_i$ is the average position vector of the i-th C$_\alpha$ atom over all time frames.

Two 40 ns long chunks from equilibrated trajectories were subjected to principal component analysis (PCA) and perturbation response scanning (PRS); see next subsections for details of these methods. The data from MD simulations were analyzed by the open-source Python package ProDy[53–56] as well as custom Python and tcl scripts. Graphics were prepared with Graphpad Prism 10.

2.2.1 Principal Component Analysis (PCA)

The MD simulations conducted in our study cover a comprehensive exploration of the protein's dynamical behavior over sub-µs timescales. Normal mode analysis (NMA) models protein as a harmonic oscillating system and determines the protein dynamics around an energetically stable state of the protein. Low-frequency vibrations, also known as low-energy modes, are associated with collective motions, whereas higher-frequency modes are linked to local deformations.[57–63] PCA is an approach for comprehending protein dynamics that involves analyzing an ensemble of conformations obtained from MD simulations.[34] The mathematical principles underlying PCA and NMA share similarities: both require solving linear equations. In PCA, the variance-covariance matrix (**C**) is diagonalized; **C** approximates the inverse of the Hessian matrix employed in NMA.[57] The covariance matrix is constructed using the analysis of multiple snapshots from an MD trajectory, rather than through the calculation of the second derivative near a selected energy minimum. In both instances, the outcomes provide insights into the potential motions a particular structure can undergo, while it samples a stable conformational state. Reducing the dimensions obtained from MD simulations can be advantageous for an unbiased global analysis and to isolate specific configurations. We used PCA to discern the dominant motions of TolC during the MD simulations. PCA calculations were carried out using ProDy[53–56] and the C$_\alpha$ atoms were subjected to this analysis. In our previous work we have shown that 40 ns chunks of equilibrated trajectories can sufficiently sample the elastic motions around a selected energy minimum of a protein.[64,65] We have therefore utilized 240-280 and 460-500 ns fragments of the MD trajectories. Extracellular loops and a part of the equatorial domain which displays large motions obscuring the motions of the overall TolC were excluded in the construction of the **C** matrix.

2.2.2 Perturbation Response Scanning (PRS)

The PRS method is a powerful tool we previously developed to identify key residues that are functional in the interconversion of one conformer of a protein into another. PRS uses linear response theory to shed light on the possible conformational changes of protein might undergo by applying external forces on residues *in silico.*[36] In previous studies,[66,67] we and others used PRS to study water-soluble proteins. However, TolC is a transmembrane protein with much larger size and requires embedding the TolC homotrimer in a lipid bilayer. Studying TolC dynamics via PRS also provided us the opportunity to evaluate the utility of this powerful method on membrane proteins and solve possible problems arising from this relatively complex environment.

PRS requires experimentally obtained initial and target coordinates of the C_α atoms of a protein, $\mathbf{S}_{\text{initial}}$ and $\mathbf{S}_{\text{target}}$, respectively. In our case, these structures were the closed and open forms of TolC. $\mathbf{R}_0$ represents the unperturbed state coordinates (initial), $\mathbf{R}_1$ represents the perturbed state coordinates (target) of the C_α atoms. The external forces vector ($\Delta\mathbf{F}$) in random directions are sequentially applied on each residue of the initial structure. Each predicts displacements in the initial structure, $\Delta\mathbf{R}_1$ by

$$\Delta\mathbf{R}_1 = \langle\mathbf{R}_1\rangle - \langle\mathbf{R}_0\rangle \approx \frac{1}{k_B T}\mathbf{C}\Delta\mathbf{F} \tag{2.10}$$

where k_B is the Boltzmann constant, and T is the absolute temperature.

A total of 250 random forces are applied to each C_α atom in the protein which results in $250N$ predicted displacement vectors, where N is the number of residues. The agreement between experimentally observed and predicted displacements of each residue i in response to the applied force is calculated by the Pearson correlation coefficient (C_i) between predicted and experimental displacements. Thus, each $\Delta\mathbf{R}_1$ for applied random forces is compared with the experimentally determined difference between $\mathbf{S}_{\text{initial}}$ and $\mathbf{S}_{\text{target}}$ coordinates ($\Delta\mathbf{S}$), averaged over all affected residues k:

$$C_i = \sum_{k=1}^{N} \frac{\left[(\Delta R_k)^i - \left(\overline{\Delta R}\right)^i\right](\Delta S_k - \overline{\Delta S})}{(N-1)\sigma_R \sigma_S} \tag{2.11}$$

ΔS_k is the experimental displacement between initial MD frame and the target conformation where $\overline{\Delta S}$ the overbar represents average displacement, and σ_R and σ_S denote the standard deviations of experimental and predicted structures, respectively. In this equation, the magnitudes of the displacements, ΔR_k, are compared with ΔS_k. C_i takes on values in the range [0,1] where a correlation greater than 0.7 refers to strong correlation with the experimentally determined conformational changes. PRS was calculated from 240-280 and 460-500 ns chunks of these 500 ns simulations. Extracellular loops and a part of the equatorial domain were excluded in PRS calculations. Since TolC is a homotrimeric outer membrane protein, we performed PRS analysis using each chain as a replica. In the end, obtained results were averaged over 6 sets of data.

2.3 Steered Molecular Dynamics (SMD) Simulations

Steered molecular dynamics (SMD) is an advanced computational technique employed to investigate the mechanical properties, conformational changes, and free energy landscapes of biomolecules. In SMD simulations, a harmonic potential is applied to specific atoms or molecular groups in a predefined direction to simulate the atomic force microscopy or optical tweezers.[68] This harmonic potential $U(r, t)$ can be expressed as:

$$U(r,t) = \frac{1}{2}k[vt - (r(t) - r_0).n]^2 \tag{2.12}$$

where k is the spring constant, r_0 is the initial position of the dummy atom that is attached the steered atom via a virtual spring, $r(t)$ is the time dependent target position of the atom, n is the pulling direction, v is the constant pulling velocity. This potential induces a steering force:

$$\mathbf{F} = -\Delta U(r,t) \tag{2.13}$$

which drives the system along a predefined pathway (n). The work done on the system during pulling process is obtained by the integration of the force over the displacement:

$$W = \int_0^\tau \mathbf{F}(t) \cdot \mathbf{v}\, dt \tag{2.14}$$

where τ is the total time of the pulling simulation. The results from SMD simulations can be analyzed using the Jarzynski equality (2.15)[69] which relates the average work done on the system to the free energy difference (ΔF) between two states.

$$\langle e^{-\beta W} \rangle = e^{-\beta \Delta F} \tag{2.15}$$

Here, $\beta = \frac{1}{k_B T}$ is the inverse thermal energy, with k_B is the Boltzmann constant and T is the absolute temperature. In constant velocity SMD simulations, the force is applied on a dummy atom which is attached to the SMD atom with a virtual spring. The dummy atom is moved with constant velocity and the force between different states is measured. The measured force data is used to calculate work done on the system.

Thus, we performed SMD calculations using the closed-form TolC structure (PDB ID: 1EK9) as the initial point[25] in separate SMD runs, carbenicillin, piperacillin, or oxacillin was positioned at the periplasmic tip of the protein by docking using the CB-Dock2 tool.[70] The charges of carbenicillin, piperacillin, and oxacillin in water are -2, -1, and -1, respectively. While these charges might shift depending on the local environment of the drugs while passing through the protein, we assumed the pKa of all positions and the charges in the drug molecules remained constant in our simulations. The simulation boxes for the membrane, protein, and three different antibiotic molecules were optimized using the CHARMM-GUI web server as described in the "MD simulations" section. Force fields for the antibiotic molecules used in our study were generated by the CHARMM general force field module of CHARMM-GUI.[46,71,72] The systems obtained with the three different antibiotics were minimized for 50,000 steps and equilibrated for 0.5 ns. A 50 kcal mol^{-1} $Å^{-2}$ harmonic spring constant was applied to a carbon atom on the hexane structure of antibiotic molecules (depicted as purple spheres in Figure 1.2C) for forcing the drug molecule to pass through the TolC channel, a value that satisfies the stiff spring approximation.[73] Antibiotics were pulled along the z-axis until they reached the extracellular loops of the protein at a constant velocity of 5 Å ns^{-1}. The molecules traveled approximately 140 Å; each SMD simulation thus lasts 30 ns. No restraints were applied to the substrates in the x and y directions. The pulling simulations of each antibiotic molecule were repeated 45 times to increase the signal-to-noise ratio. The average work done to reach the extracellular side was then calculated for each antibiotic molecule.

2.4 Bacterial Strains and Growth Conditions

Escherichia coli (*E. coli*) cells were grown at 37°C in a M9 minimal medium supplemented with 0.4% glucose and 0.2% amicase. The BW25113 *E. coli* strain (Coli Genetic Stock Center Number - CGSC No.: 7636) and the *ΔtolC732::kan E. coli* strain (CGSC No.: 11430)[74] were previously prepared in the Toprak Lab as described before.[75]
Using the method from reference[76], we removed the kanamycin resistance marker in the *ΔtolC732::kan E. coli* strain. In the article, we refer to the *E. coli* strain *tolC* gene deletion as *ΔtolC* strain.

The *tolC* gene from BW25113 (wild type, WT) strain was polymerase chain reaction (PCR) amplified using:

5′-ATTCAAAGGAGGTACCCACCATGA AGAAATTGCTCCCCATTC-3′ (forward), and
5′AGAAATCGATTGTATCAGTCTCAGTTACGGAAAGGGTTATGAC-3′ (reverse)
primers. PCR amplified *tolc* gene was then cloned into the pSF-Oxb14 plasmid which was obtained from Oxford Genetics (OGS557, Sigma) using the NEBuilder HiFi DNA Assembly kit (New England Biolabs); by strictly following the protocols recommended by the manufacturers. The resulting plasmid (pSF-Oxb14-*tolC*) contains kanamycin resistance cassette and an Oxb14 constitutively open promoter region. The introduced *E. coli tolc* gene sequence was confirmed by Sanger sequencing.

Whole gene saturation mutagenesis library (SML) for each codon in the *tolC* gene used in our experiments was previously prepared in the Toprak Lab as described before.[75] The *tolC* mutant library were cloned into the pSF-Oxb14 plasmid and transformed into *ΔtolC* strain for downstream selection experiments. We refer to this library as TolC-SML. We refer the *ΔtolC* strain supplemented with the pSF-Oxb14-*tolC* plasmid as *ΔtolC*+p*tolC*. All selection experiments were conducted with minimal M9 media containing 50 µg/ml of kanamycin to prevent loss of the pSF-Oxb14-t*olC* plasmid.

2.5 Determination of minimum inhibitory concentrations (MIC)

Bacterial cells were overnight grown and optical densities (OD600) of cultures were measured in a 1 cm pathlength cuvette. OD600 was then adjusted to 0.001 for which corresponds ~5x10^5 colony forming unit (CFU) per milliliters. Bacterial cells were then grown in 96 well plates (~200 µl per well) in which drug gradients were created using serial dilutions (Figure 2.1A).

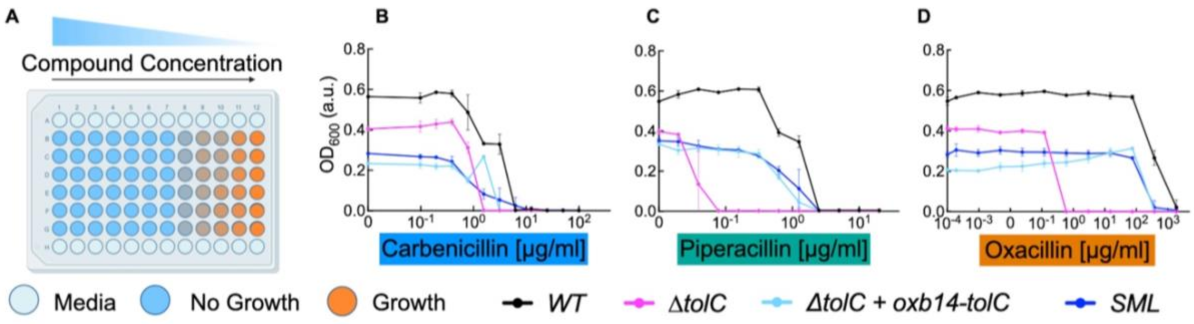

Figure 2.1 | Minimum inhibitory concentration (MIC) measurements. A. MIC assay plate setup. Blue wells indicate no growth; color gradation towards orange indicates the level of growth. (B-D) Three different antibiotics were used as selection factors. We incubated three strains and the Single Mutation Library (SML, Methods) in the presence of increasing drug concentrations and monitored bacterial growth for ~18h. We used blue x-axis label for carbenicillin, green x-axis label for piperacillin, and orange x-axis label for oxacillin. This coloring scheme representing the antibiotics was maintained throughout the manuscript. Black line represents dose response curves for wild type (BW25113) *E. coli* strain. Magenta lines represent *E. coli* strain with *tolC* gene deletion (*ΔtolC*). Cyan lines represent *ΔtolC*+pOxb14*tolC*. Blue lines represent SML strain which contains all possible amino acid mutations. Background-corrected OD600 values after 18 hours of incubation measure cell growth on the y-axis, with error bars showing standard deviations across three replicates per concentration. Raw data table can be found Table 2.1.

Highest starting antibiotic concentrations on these plates were 100 µg/ml for carbenicillin, 20 µg/ml for piperacillin, and 1875 µg/ml for oxacillin. The dilution factor for carbenicillin and piperacillin was 1/2 while it was 1/5 for oxacillin. These 96-wells were incubated for 18 hours in a humidity-controlled shaker operated at 37°C and 400 rotation per minute (RPM). After the overnight incubation, cell densities were measured using a plate reader (VictorX, PerkinElmer). The experiments were performed in triplicates for each antibiotic molecule. For each strain and antibiotic compounds, the MIC value was defined as the lowest antibiotic concentration at which the final OD600 was below ~0.04 after background correction.

Table 2.1 | Raw data of cell growth to plot Figure 2.1.

CBC 100 µg/ml	***WT***			***ΔtolC***			***WT ΔTolC+ oxb14 tolC***			***SML***		
100	0	0.002	0.002	0	0.001	0.002	0.001	0.002	0.002	0.001	0.001	0.002
50	0.001	0.002	0.002	0.001	0.001	0.002	0.001	0.002	0.002	0.001	0.001	0.002
25	0.001	0.002	0.002	0.001	0.002	0.001	0.001	0.002	0.002	0	0.001	0.002
12.5	0.002	0.02	0.003	0.001	0.002	0.002	0.002	0.002	0.003	0.001	0.002	0.002
6.25	0.002	0.003	0.003	0.001	0.002	0.002	0.002	0.002	0.002	0.001	0.002	0.072
3.125	0.356	0.359	0.272	0.001	0.002	0.001	0.002	0.002	0.002	0.001	0.042	0.117
1.5625	0.326	0.336	0.334	0.001	0.002	0.002	0.277	0.261	0.263	0.078	0.06	0.109
0.78125	0.398	0.573	0.489	0.283	0.337	0.315	0.154	0.168	0.135	0.145	0.156	0.153
0.390625	0.599	0.573	0.567	0.454	0.44	0.422	0.237	0.225	0.202	0.214	0.252	0.263
0.1953125	0.589	0.588	0.581	0.448	0.436	0.403	0.232	0.222	0.203	0.257	0.266	0.27
0.09765625	0.587	0.544	0.544	0.446	0.41	0.393	0.245	0.225	0.213	0.269	0.256	0.278
0	0.562	0.567	0.563	0.417	0.396	0.402	0.258	0.227	0.214	0.282	0.284	0.284
PIP (20µg/ml)	*WT*			*ΔtolC*			*WT ΔTolC+ oxb14 tolC*			*SML*		
20	0.005	0.004	0.004	0	0.001	0.001	0.001	0.001	0.002	0.002	0.003	0.003
10	0.004	0.004	0.005	0.002	0.002	0.002	0.001	0.002	0.002	0.003	0.003	0.004
5	0.003	0.005	0.005	0.001	0.001	0.002	0.001	0.002	0.002	0.004	0.003	0.003
2.5	0.003	0.005	0.005	0.001	0.002	0.002	0.001	0.002	0.003	0.003	0.003	0.003
1.25	0.35	0.316	0.374	0.002	0.002	0.002	0.049	0.06	0.027	0.146	0.005	0.188
0.625	0.372	0.399	0.408	0.001	0.002	0.001	0.174	0.179	0.157	0.198	0.186	0.226
0.3125	0.597	0.605	0.621	0.002	0.002	0.002	0.264	0.309	0.286	0.278	0.267	0.284
0.15625	0.614	0.613	0.603	0.002	0.002	0.002	0.268	0.322	0.303	0.305	0.303	0.309
0.078125	0.601	0.587	0.594	0.002	0.002	0.002	0.278	0.324	0.317	0.307	0.31	0.313
0.0390625	0.605	0.609	0.612	0.01	0.046	0.349	0.299	0.317	0.331	0.305	0.316	0.357
0.01953125	0.598	0.562	0.59	0.375	0.383	0.392	0.298	0.285	0.327	0.342	0.33	0.37
0	0.55	0.551	0.543	0.4	0.38	0.411	0.334	0.326	0.344	0.339	0.358	0.359
OXA (1875 µg/ml)	*WT*			*ΔtolC*			*WT ΔTolC+ oxb14 tolC*			*SML*		
1875	0.001	0.001	0.064	0.0001	0.0001	0.0001	0.0001	0.0001	0.0001	0.02	0	0
375	0.225	0.294	0.279	0.0001	0.0001	0.0001	0.004	0.003	0.01	0.001	0.06	0.001
75	0.577	0.558	0.567	0.001	0	0	0.31	0.323	0.306	0.27	0.26	0.268
15	0.576	0.588	0.555	0.002	0	0	0.295	0.313	0.267	0.286	0.278	0.305
3	0.589	0.597	0.572	0	0.003	0	0.285	0.256	0.246	0.286	0.273	0.304
0.6	0.579	0.57	0.58	0	0	0.001	0.247	0.261	0.224	0.275	0.288	0.308
0.12	0.598	0.595	0.593	0.388	0.393	0.395	0.255	0.245	0.217	0.282	0.285	0.317
0.024	0.585	0.6	0.573	0.392	0.395	0.411	0.223	0.25	0.201	0.28	0.287	0.318
0.0048	0.576	0.587	0.572	0.388	0.388	0.4	0.213	0.245	0.209	0.288	0.298	0.324
0.00096	0.592	0.588	0.589	0.396	0.405	0.427	0.201	0.202	0.202	0.278	0.285	0.31
0.000192	0.559	0.574	0.562	0.402	0.401	0.422	0.203	0.201	0.21	0.283	0.292	0.34
0	0.554	0.525	0.562	0.403	0.406	0.425	0.201	0.207	0.21	0.268	0.293	0.289

2.6 Selection Assay

We used three antibiotics: carbenicillin, piperacillin, and oxacillin as selection agents. We used the saturation mutagenesis library (SML) for *tolC* that we previously reported in a publication.[75] In this library, all residues except start codon (471 residues in the mature TolC protein, and the 22 residue-long signal sequence) were mutated to all other possible residues, and a pool of mutant library was generated (Figure 2.2). We measured the fitness effects of mutations under selection using a liquid-based sequencing assay. Our assay does not allow us to evaluate the expression levels or stability of thousands of TolC mutants. However, by completing the screen with three different antibiotics, we can confidently deduce that a TolC mutant is expressed and stable enough if the relative fitness of the mutant under the selection with at least one antibiotic, with respect to the wild-type TolC, is non-deleterious, suggesting that the efflux for at least one antibiotic is still occurring.

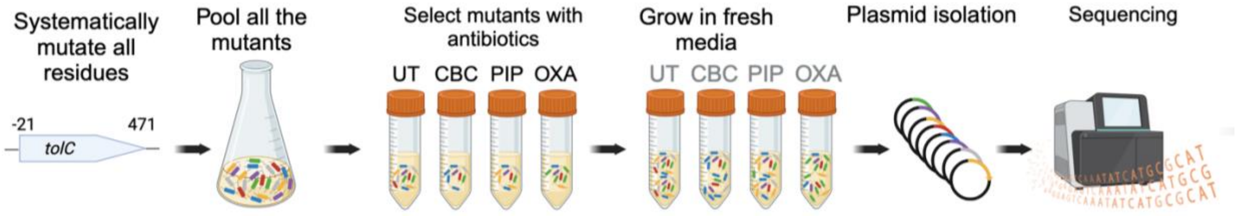

Figure 2.2 | Selection assay protocol. We conducted deep mutational scanning on TolC, systematically mutating all 493 residues, which includes the 21-amino acid long signal sequence preceding the start codon (excluding it). Residues were mutated to all the 19 other amino acids, along with the stop codon. Obtained mutants were pooled together and grown overnight. Overnight grown mutant pool and *ΔtolC* strains were split into cultures: untreated (UT), CBC, PIP, OXA; the experiment was replicated once. Cultures other than the untreated were treated with the relevant selection factors. Cultures were exposed to drugs for 3 hours for selection. This was followed by 6 hours long incubation in fresh growth media without any selection agent for the recovery of cells (gray abbreviations on the tubes represent previously applied antibiotics). We isolated *tolC* mutant carrying plasmids and PCR amplified the *tolC* gene for amplicon sequencing. Mutation frequencies were calculated by deep sequencing and fitness values of each mutation were calculated formula in (2.12).

$$Fitness_{mutant} = \log_{10}\left(\frac{Count_{Mutant}^{Treated}}{Count_{WT}^{Treated}}\right) - \log_{10}\left(\frac{Count_{Mutant}^{Untreated}}{Count_{WT}^{Untreated}}\right) \tag{2.12}$$

We grew the mutant library in M9 minimal medium supplemented with 0.4% glucose and 0.2% amicase overnight, diluted to a final optical density of 0.001, and then exposed these cultures to one of the selection factors: carbenicillin, piperacillin, and oxacillin for 3-hour at 37°C, 400 RPM. In parallel, we grew cultures without any selection UT for separating drug-induced fitness effects from other potential fitness effects that are not related with the bactericidal effects of antibiotics. The concentrations for these antibiotics in this selection assay were 20 µg/ml and 10 µg/ml for carbenicillin, 10 µg/ml for piperacillin, and 460 µg/ml for oxacillin. These concentrations were close to the MIC of the related compound (Figure 2.1B-D). We note that for carbenicillin we used two carbenicillin concentrations because the dynamic range of the fitness values was not large enough when the selection was done with the lower concentration. The dose-response curve for carbenicillin is very steep (higher Hill coefficient), making it difficult to adjust the selection strength.

At the end of the selection period, these cultures were spun down at 5000xg for 5 minutes. The pellets obtained from spinning were resuspended in fresh M9 minimal medium supplemented with 0.4% glucose, 0.2% amicase and 50 µg/ml kanamycin and incubated at 37°C, 400 RPM for 6 hours to increase cell density and ensure harvesting of enough *tolC* carrying plasmid for sequencing. We recorded cell densities during this recovery period as depicted in Figure 2.3.

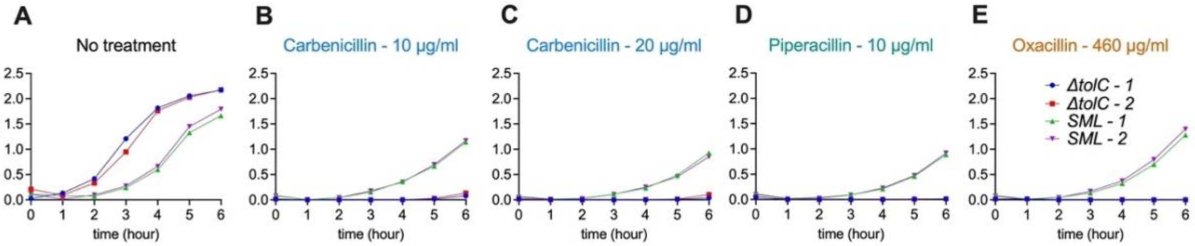

Figure 2.3 | Growth curves after the selection agent incubation. After the 3-hour selection agent incubation, surviving cells from *ΔtolC*, *SML*, and their replicate cultures were transferred to fresh M9 minimal media. The growth of these cells was monitored for 6 hours. Cultures for no treatment case were grown properly. *SML* cultures containing plasmids in their cells started to grow properly after 3 hours of incubation in fresh media. In contrast, *ΔtolC* cultures did not show growth within the represented period, suggesting the importance of the *tolC* gene for survival in the presence of these antibiotics. Blue and red colors represent *ΔtolC* cultures and green and magenta colors represent *SML* cultures.

Cells were harvested by spinning cultures at 5000xg for 5 minutes. Pellets were collected for plasmid purification. *tolC* gene variants on these plasmids were amplified with PCR using:
5’-TACCCGGCAGATCTTTGTCGATCCTA-3’(forward), and
5’-GTGAGCTGAAGGTACGCTGTATCTCA-3’ (reverse) primers.

These products were sequenced on Illumina NovaSeq 6000, producing 151 bp reads. Sequence reads were compared with the wild type *tolC* sequence and mutations were listed. Sequence reads that had mutations in more than one residue were excluded from the analysis. Synonymous mutations yielding the same amino acid replacement were grouped together and used as a reference for relative fitness calculations. The frequency of each mutation was calculated by dividing the number of counts for that mutation with the number of all reads, including alleles with multiple mutations.[75] We then used the formula displayed in Figure 2.2 to calculate relative fitness effects of each mutation.

3. RESULTS

3.1 TolC Dynamics are Inherently Optimized for Efflux

We performed MD simulations to gain insights about TolC structural dynamics for closed and open states of the wild type TolC. RMSD of TolC during these simulations was calculated as overall deviation from the initial structures. The deviations of protein C_α atoms were around 2 – 4 Å which shows us the conformational drifts of the protein were stable during the simulations (Figure 3.1A).

RMSFs were highest at the periplasmic side for simulated closed and open structures (Figure 3.1B; green shaded region). However, the fluctuations were greater on the periplasmic side in the open form, and on the outer membrane side in the closed form, which might be indicative of the changes in the closing/opening motion of the protein (Figure 3.1B). Finally, the larger fluctuations near residue 200 correspond to the equatorial domain helices in the widest region of the protein contacting water and are not functionally relevant. Consequently, their mobility remains the same irrespective of the open/closed forms.

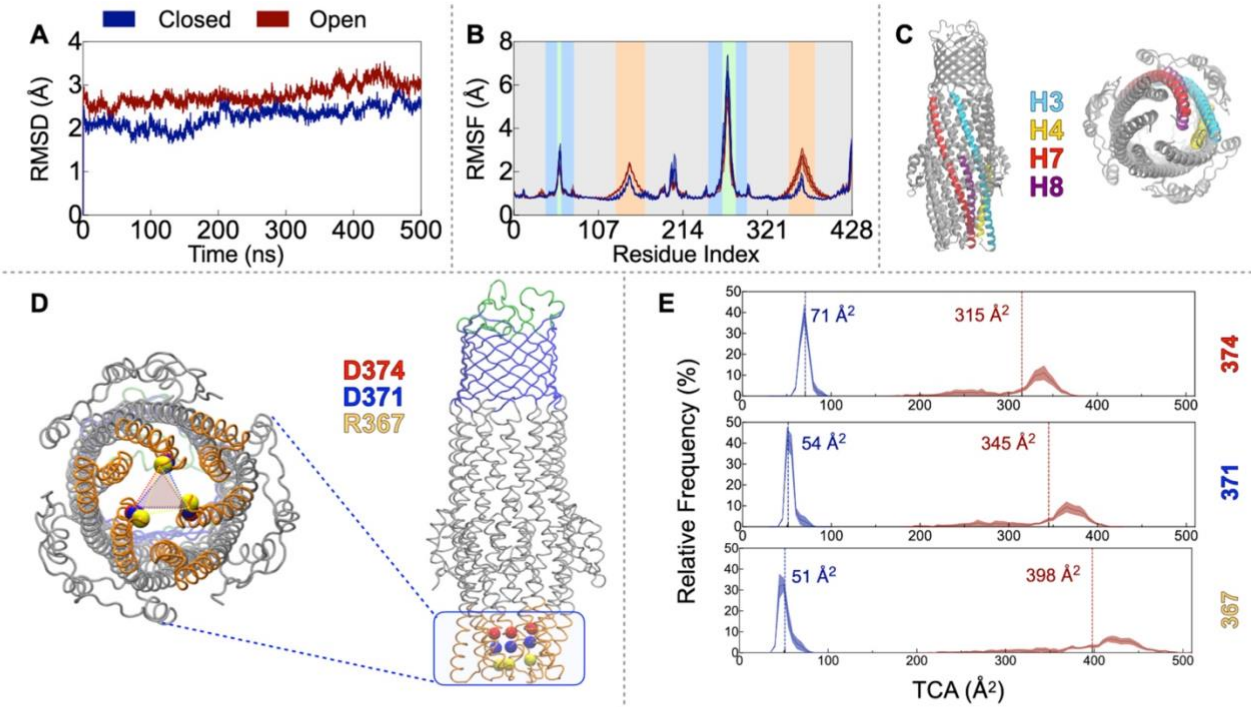

Figure 3.1 | Molecular dynamics of ligand-free TolC. A. C_α RMSDs of TolC remain in the 2-4 Å range during the 500 ns MD trajectories of both closed (blue), and open (red) forms. B. C_α RMSFs; colored vertical stripes follow the coloring of the TolC regions Figure 1.1B: green extracellular loops, orange periplasmic entry region, blue β-barrel, gray the rest. Standard error of the mean (SEM) obtained from the average of the three chains in the trimer are shown as shades. C. Specific four helices of one TolC protomer highlighted; side and bottom views; residue indices: H3 cyan (78-145), H4 yellow (151-185), H7 red (297-363), and H8 magenta (369-403). D. Selected pore constricting trimeric C_α atoms visualized as spheres on the protein (R367 yellow, D371 blue, D374 red); the bottom view highlights the triangular shape. E. Triangular cross-sectional area (TCA) histograms of residues in D.

The greatest conformational changes were observed in the H7/H8 helices (the helix numbering is shown in figure 3.1C.). H3/H4 helices were comparatively stable (Figure 3.1C).[26,77,78] D371 and D374 on H8 are at the points of the two of the narrowest constrictions.[77] In fact, D371 was shown to be important in gating, with increased susceptibility to various substances in the D371V mutant. R367 is another site that makes strong interactions to hold inter-protomer and intra-protomer helices together (R367-D153 and R367-T152 for the former and Y362-D153 for the latter).[29] Since TolC is a homotrimer, we calculated the triangular cross-sectional area (TCA) using the C_α atoms of these specific residues, R367, D371, and D374, which form a ladderlike entry region into the pore used in efflux (Figure 3.1D). TCAs for the open structure are expectedly much larger than the closed form. However, the largest area is at the level of the innermost D374 residue in the closed form while the reverse is true for the open form, i.e., the truncated cone formed by these three residues is reversed during opening (Figure 3.1E).

To understand the underlying motions that collectively orchestrate TolC dynamics in the absence of drugs, we monitored the principal components (PCs) obtained from the trajectories. Our aim for doing these calculations was to check if the collective modes describe intrinsic motions with a clear directionality from the periplasmic to the extracellular side, so that even in the absence of AcrAB in our model, TolC would provide relevant information for efflux. The top three PCs have similar amounts of contributions to the dynamics in the closed form, while the most collective mode of motion is more separated than the rest in the open form (Figure 3.2A).

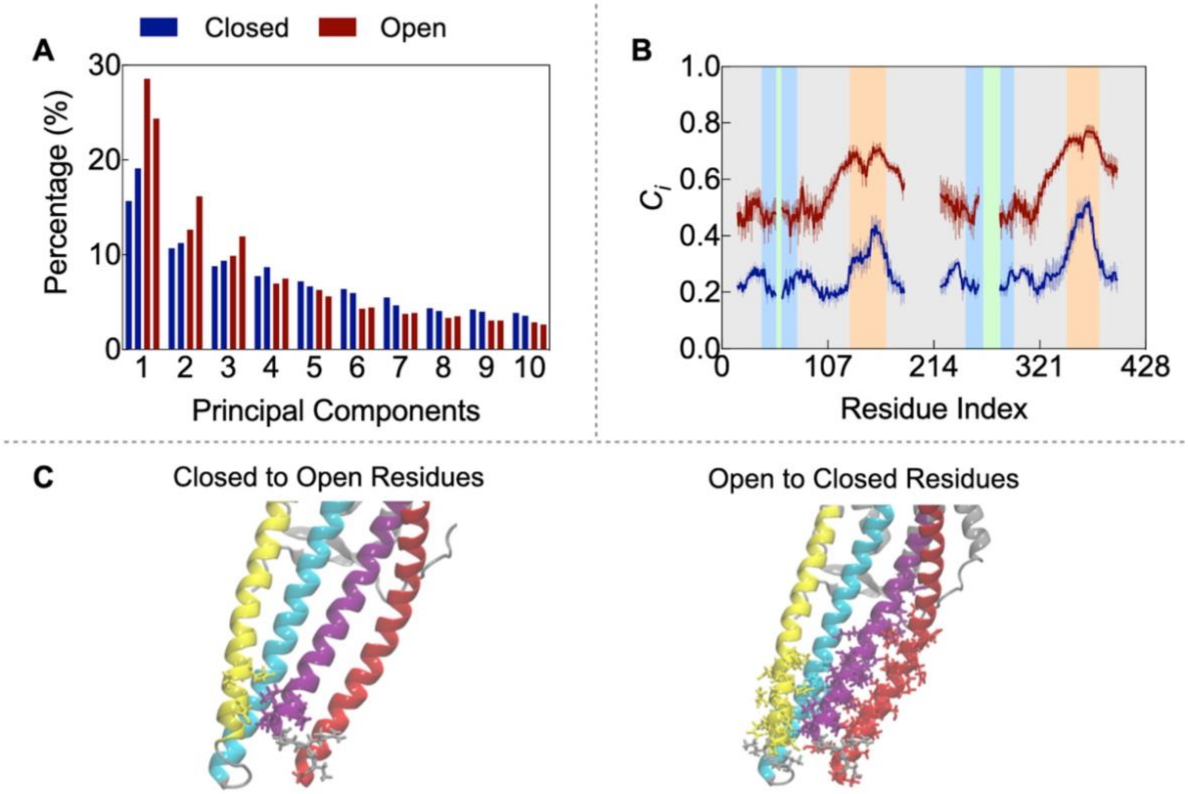

Figure 3.2 | Collective motions of TolC. A. Contribution of the top 10 PCs, obtained from two separate trajectory pieces (240-280 ns and 460-500 ns) in each of the closed (blue) and open (red) form simulations. B. Correlation coefficients obtained from PRS for closed and open forms. SEM shown as shades. Highest mobility regions excluded in the construction of the correlation matrix to capture motions of the main structure appear as disconnected regions in the graphs. C. PRS determines single residues implicated in channel opening mainly located on four helices shown in C. Top-ranked residues for opening (C_i>0.50): 160, 366-369, 369-374; top-ranked residues for closing (C_i>0.70): 129,132,133,135-137,140,149,150,152-164,341-377. D371 has the highest correlation value of 0.54 and 0.82, respectively for closed and open forms.

In its closed form, the primary motion (PC1) induces a torque along the efflux axis in the lower half and a stretching opening in the upper half; the reverse is true for PC2. PC3 is an upward pumping motion (see Supplementary Videos 1-3). In the open form, motions in the open periplasmic side overwhelm the dynamics, while PC2 and PC3 overlap with the top two PCs of the closed form (see Supplementary Videos 4-6). Thus, TolC remains primed for efflux even in the absence of drugs, more so when closed than open.

PRS calculations determined the key residues involved in triggering the open-to-closed and closed-to-open conformational changes (Figure 3.2B-C). Our findings show that the closed-to-open correlation coefficients, C_i, are significantly lower than open-to-closed ones, suggesting the protein naturally tends to close from an open state and requires specific residue perturbations for opening from a closed state. Despite the less stringent selection of the threshold we employed, we found far fewer residues that can enforce channel opening. Moreover, residues located on the H7/H8 helices have higher C_i values than the H3/H4 helices, reinforcing the active role of the former pair of helices in channel opening as previously reported.[26,77] Aligning with previous findings, our results confirmed the closed form as TolC's stable state, upon which we based the rest of our simulations.

3.2 Dynamic Changes in a Critical Interaction Network Facilitate Drug Efflux through TolC

TolC protein is known for the expulsion of the various antibiotic molecules including carbenicillin, piperacillin, and oxacillin.[23] We used steered molecular dynamics (SMD) simulations to track the work produced as antibiotics move through TolC. We note that the general trends and the energy levels in the work curves did not change when the pulling atom was modified to the nitrogen atom in the middle of the carbenicillin molecule from the carbon atom on the hexane ring. Thus, our SMD atom is a carbon atom on the hexane ring which is common in all three antibiotic molecules. Reducing the pulling velocity on carbenicillin molecule 10-fold, to 0.5 Å ns^{-1} from 5 Å ns^{-1}, did not change the profiles in the first 30 Å of the pump. As the molecule moves through inside of the hollow part of the protein, the work required to pull is reduced; the slope of $m_3<m_2<m_1$ (Figure 3.3).

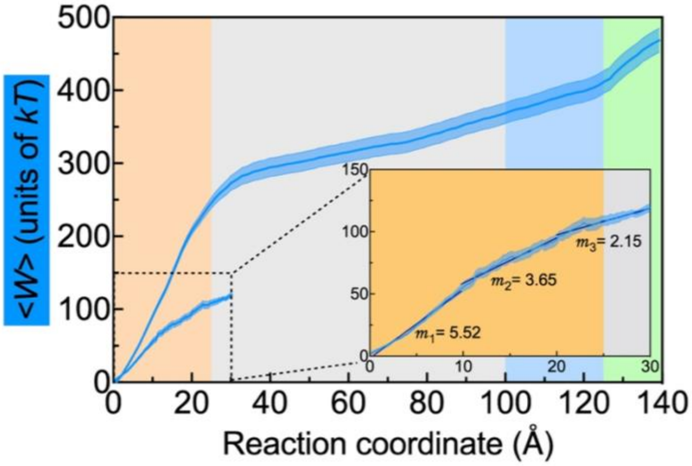

Figure 3.3 | Work curve comparisons of 5 Å ns^{-1} and 0.5 Å ns^{-1} (inset) pulling velocities.

We calculated the average work to transport from the periplasmic to the extracellular side, with the order being carbenicillin > piperacillin > oxacillin (Figure 3.4A). We also monitored the drug-protein interactions along this path (Figure 3.4B-D). We found common interactions for all antibiotic molecules we tested at the extracellular side during the final exit of the antibiotic (those in the green stripe region in Figure 3.4). However, carbenicillin formed more bonds than the other antibiotics, correlating with our findings that its efflux rate through *E. coli* TolC is lower. The rise in hydrogen bonds during carbenicillin's transfer increased energy expenditure, prompting us to explore if this was due to direct contacts with TolC. Our analysis revealed that the average number of hydrogen bonds with TolC's pore lining and the derivative of average work shared similar patterns, albeit with a slight shift in the reaction coordinate (Figure 3.4B). This shift results from basing the reaction coordinate on the pulling atom (purple in Figure 1.2C), in contrast to counting hydrogen bonds from any part of the drug molecule and TolC.

Residues that formed two or more hydrogen bonds with selected antibiotics were mainly clustered at the periplasmic tip of the protein (Figure 3.4C). For carbenicillin, the polar residues lining the pore played an important role in retarding the progress of the drug movement. Moreover, the hydrophobics at the entry region seemed to form a barrier for carbenicillin but not for piperacillin and oxacillin. The lack of this initial barrier might be the main reason behind the efficient efflux of oxacillin and why it is a nonviable drug for treating Gram-negative infections (Figure 2.1 and

Figure 2.3). Once the antibiotic molecules overcame the resistance to move at the TolC entrance region marked by the orange regions in Figure 3.4, they accessed the membrane bound part of the pore with relative ease.

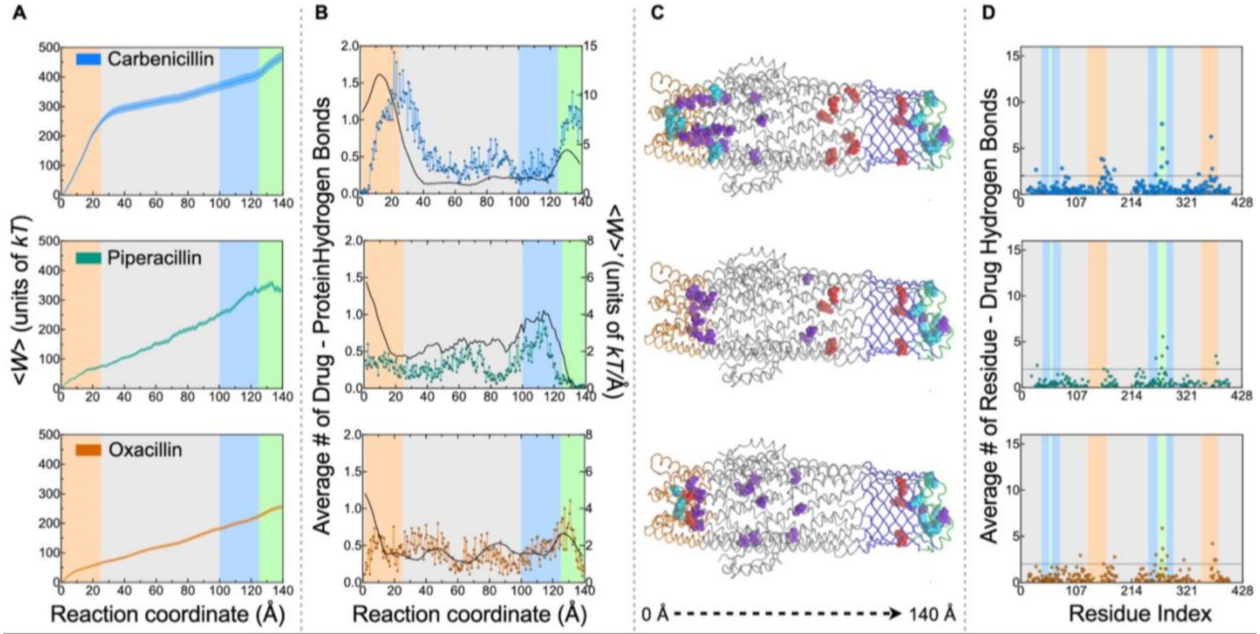

Figure 3.4 | Mapping drug-TolC interactions. Carbenicillin (blue; top row), piperacillin (green; middle row), oxacillin (yellow; bottom row). Vertical stripes use the color code of the regions of TolC depicted in Figure 1.2B. A. The work curves from SMD simulations. B. The average number of hydrogen bonds between drug and TolC along the reaction coordinate (colored; left y-axis) and the first derivative of the work (black; right y-axis). C. Residues that have more than an average of two hydrogen bonds (above dashed line in D) plotted on the 3D representation of the protein; charged residues red, polars purple, and hydrophobics cyan. D. Number of hydrogen bonds formed between a given residue and the drug averaged over 45 SMD simulations.

To check if the results depend on the biases introduced by SMD simulations, we also carried out free MD simulations with these molecules, following the work in a previous study.[32] We placed carbenicillin molecule freely in three regions of the protein: entry, transfer, and exit. In total, 9 classical MD simulation runs each of 100 ns length were performed with these structures. The RMSD of C_α atoms for these simulations, and the number of hydrogen bonds in each region during the simulations are shown in the Figure 3.5A-B.

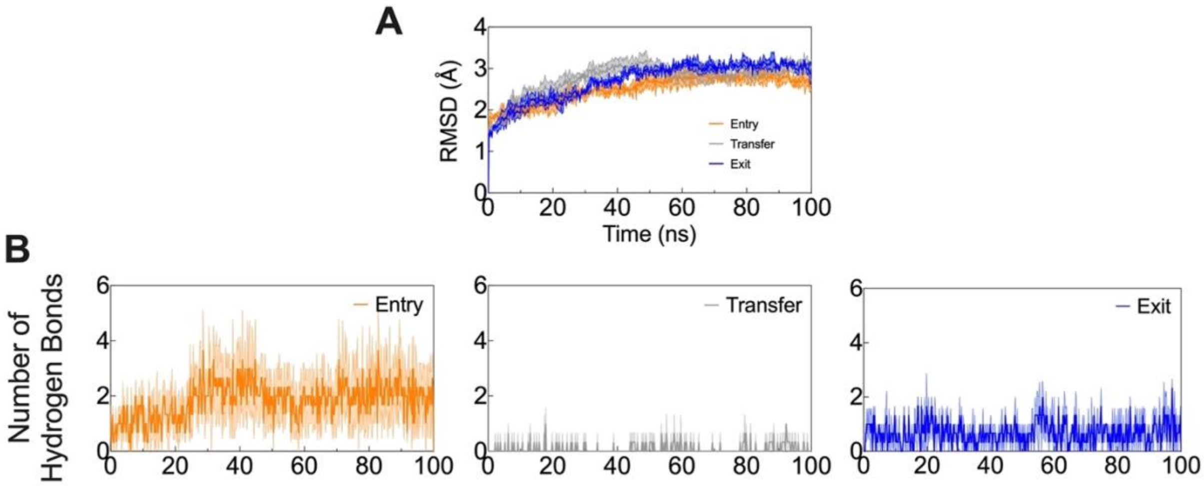

Figure 3.5 | Free MD simulations with carbenicillin placed at different positions along the pump. A. RMSD graph for TolC C_α atoms. B. Average number of hydrogen bonds during the 100 ns simulations with three replicates. SEM of the three simulations are shown as shades.

According to these "free MD simulations" by placing carbenicillin at different locations along the closed form of protein, we found that TolC-carbenicillin hydrogen bond densities are the largest in the entry region, very few occur in the transfer region and approximately the one hydrogen bond is maintained by carbenicillin throughout the simulation in the exit region. These occurrences are similar to what we had observed in SMD simulations. Residues display larger than 5% occupancy at least one of the simulations are displayed in Table 3.1.

Table 3.1 | Carbenicillin – TolC hydrogen bond occupancies during "free MD simulations". Occupancies greater than 100 % indicate there is more than one hydrogen bond between drug and the indicated residue.

ENTRY	Run - 1	Run - 2	Run - 3	AVERAGE
367	111.0%	5.4%	124.4%	80.3%
143	122.4%	47.4%	0.0%	56.6%
366	0.0%	0.0%	61.8%	20.6%
362	22.8%	0.2%	0.0%	7.7%
369	22.2%	6.4%	0.4%	9.7%
152	0.0%	0.0%	19.4%	6.5%
368	5.4%	0.0%	0.0%	1.8%

TRANSFER	Run - 1	Run - 2	Run - 3	AVERAGE
30	0.00%	6.20%	0.00%	2.10%

EXIT	Run - 1	Run - 2	Run - 3	AVERAGE
283	39.4%	26.8%	39.4%	35.2%
68	2.4%	6.2%	8.6%	5.7%
257	4.0%	6.0%	4.6%	4.9%
66	4.0%	3.2%	5.6%	4.3%
281	6.0%	1.2%	4.0%	3.7%
274	6.8%	4.0%	0.2%	3.7%
261	3.8%	5.0%	1.4%	3.4%

The only one with significant overlap which was not observed in our SMD simulations (Figure 3.4D) is R143 which is at the periplasmic tip of TolC and is below our docking position for SMD simulations. Therefore, the drugs pulled in SMD simulations are never in contact with this residue.

We next looked more carefully at the movement of carbenicillin through the protein channel since it experiences a larger number of interactions at the entry to the protein than the other antibiotics and forms extra hydrogen bonds with charged residues in the extracellular barrel region (suggested by the middle peak in Figure 3.4B). While carbenicillin was moving through the first ~30 Å long region, the triplet salt bridges between R367 and D153 were typically broken. Interestingly, a permanent salt interaction with D371 is established instead (Figure 3.6A).

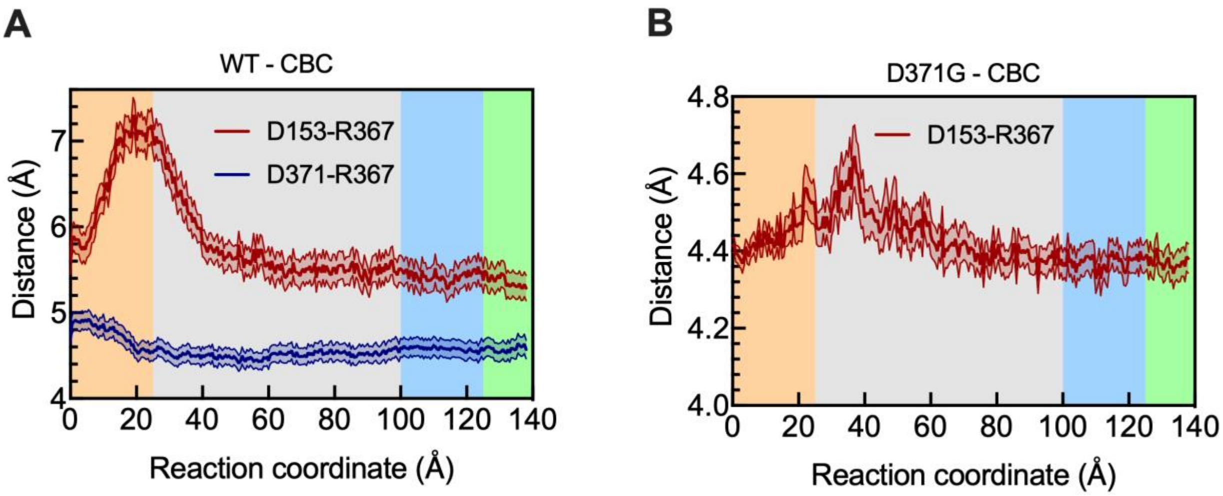

Figure 3.6 | Critical salt bridge distances for R367. A. The average donor-acceptor distance for R367 with D371 and D153 residues show that the salt bridge is disrupted until carbenicillin moves past the first 30 Å and is then reestablished. B. The donor-acceptor distance is much more stable than the WT in the case of the D371G mutation. Averages of 45 SMD simulations and the three chains in TolC are shown with SEM.

Here, the negatively charged carbenicillin competed with D153/D371 on the H2/H7 helices. Once carbenicillin went beyond this region, the drug molecule moved predominantly unhindered through the next 90 Å. In fact, the charged and polar residues aided this last part of the journey by making a hand-over-hand type of coordinated motion that advanced the drug to the outer region of the channel. Finally, in the last ~25 Å, the drug overcame the hydrophobic network of interactions that seal the exit before it finally left the channel.

3.3 Deep Mutational Scanning of TolC Reveals Mutations Disrupting Dynamical Interaction Network and Hindering Efflux

We employed deep mutational scanning (DMS) to differentiate the fitness effects of mutations in TolC across three different antibiotics. This high-throughput technique allowed for comprehensive analysis of how specific mutations impact antibiotic sensitivity and efflux efficiency. Using a sequencing-based selection assay, we quantified the fitness impact of single amino acid substitutions across TolC, with carbenicillin, piperacillin, and oxacillin as selection agents.

The relative fitness histograms illustrate distribution of relative fitness values for mutations under different antibiotic treatment, providing insight into how specific mutations impact the function and efficiency of the efflux pump under the presence of various antibiotics. The relative fitness values centered around 0.0 indicating that most mutations have a neutral effect on fitness with these antibiotics (Figure 3.7). Also, we can deduce that most of the mutation does not disrupt the efflux.

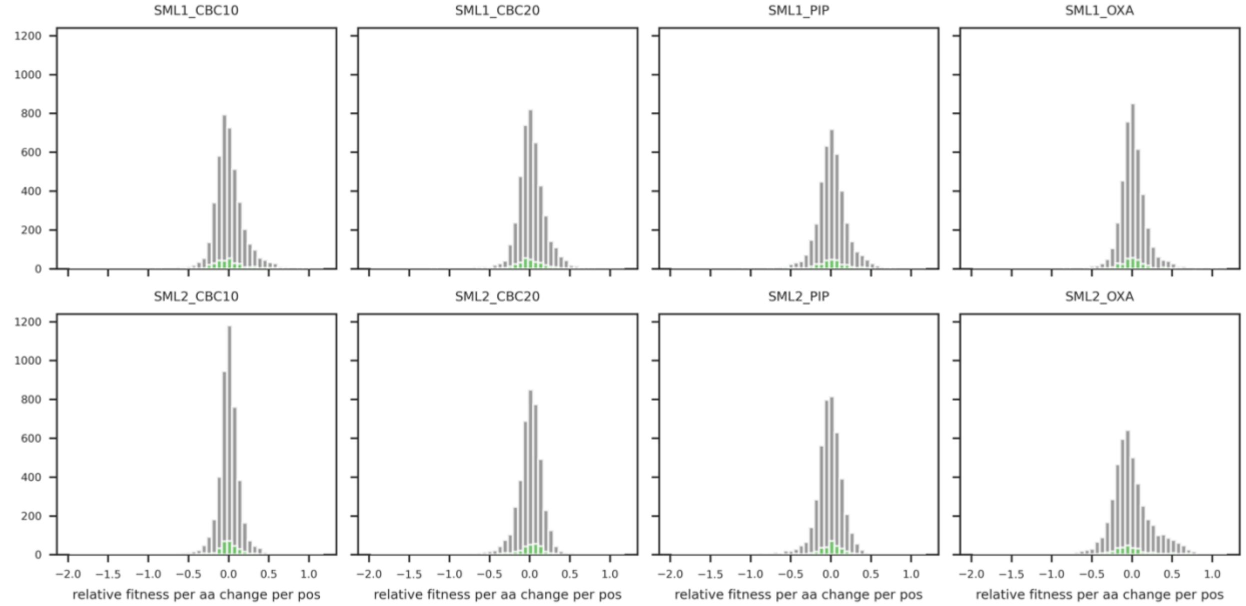

Figure 3.7 | Relative fitness histograms. Grey histograms show the distribution of relative fitness measurements of all amino acid changes detected in the corresponding sample and replica. Green overlayed histograms show the distribution of relative fitness measurements of synonymous mutations. Relative fitness is defined as the log10 value of fraction of a mutant allele in the drug treated sample divided by the untreated.

Scatter plots in significance tests at 2.5σ show the relative fitness measurements of the same amino acid changes in two biological replicates. 2.5σ from the center covers about 99.4% of the data. Blue and red colored dots in Figure 3.8 fall in the extreme tails of the distribution.

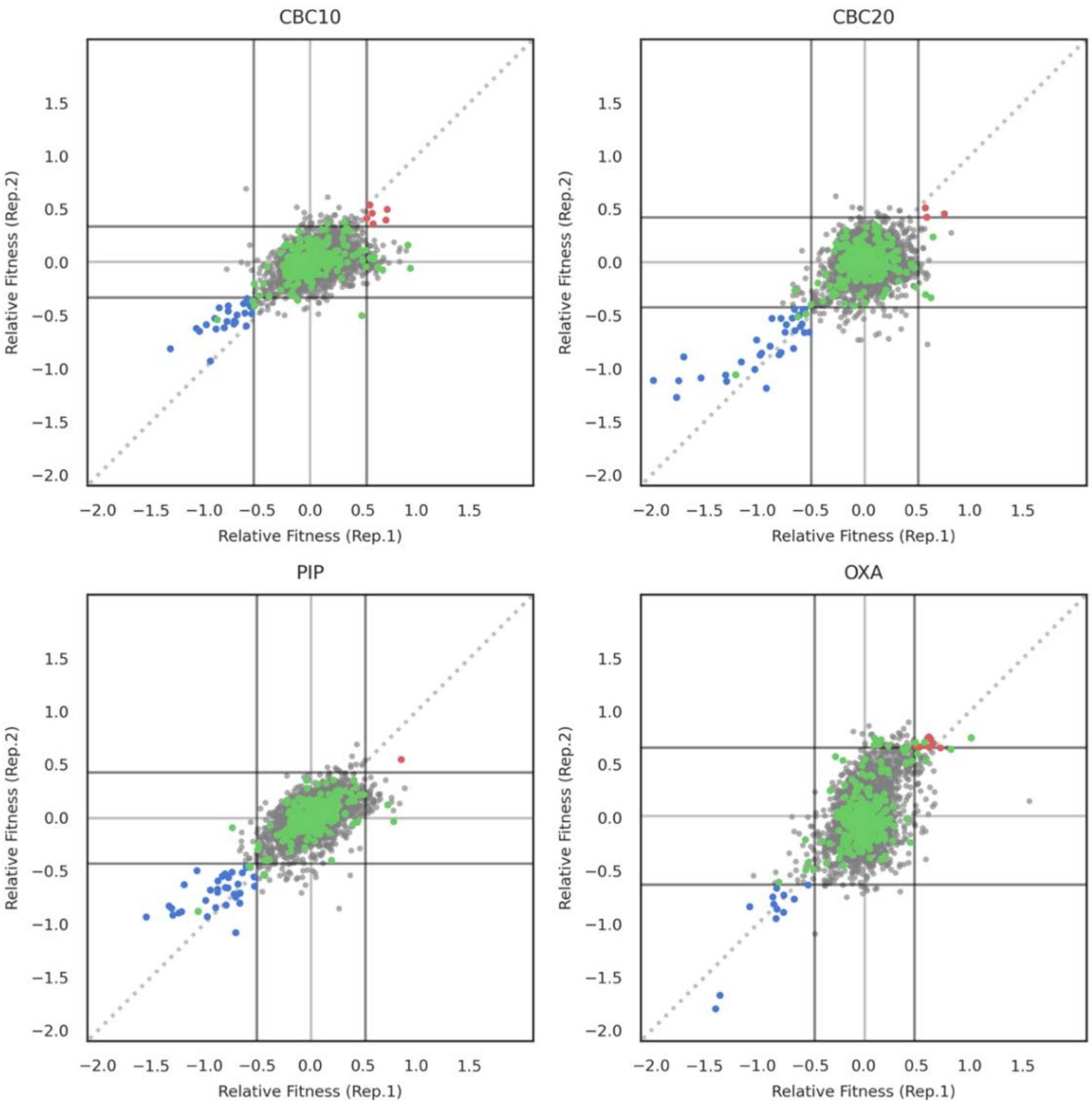

Figure 3.8 | Significance tests at 2.5σ of both samples (approximately 99.4 % confidence interval). Grey dots represent all mutant alleles and green dots represent synonymous mutant alleles. A significance threshold of 2.5 standard deviations of synonymous mutation relative fitness distribution in both replicates is used to determine significantly resistance and sensitivity conferring mutations, indicated in red and blue, respectively.

TolC protein tends to gain sensitivity conferring mutations rather than resistance conferring ones which confirms its well-adapted efflux activity (Figure 3.8).

Scatter plots show the relative fitness measurements of the same amino acid changes across different drug selections. The mean relative fitness of two biological replicates represents each mutant allele. Significantly selection conferring mutations for both drugs were mostly overlapping for carbenicillin and piperacillin. Conferring sensitivity against oxacillin relatively harder than the other two drugs. Although, the sensitivity conferring mutations for oxacillin and other two were also overlapping in the relative fitness measurements (Figure 3.9).

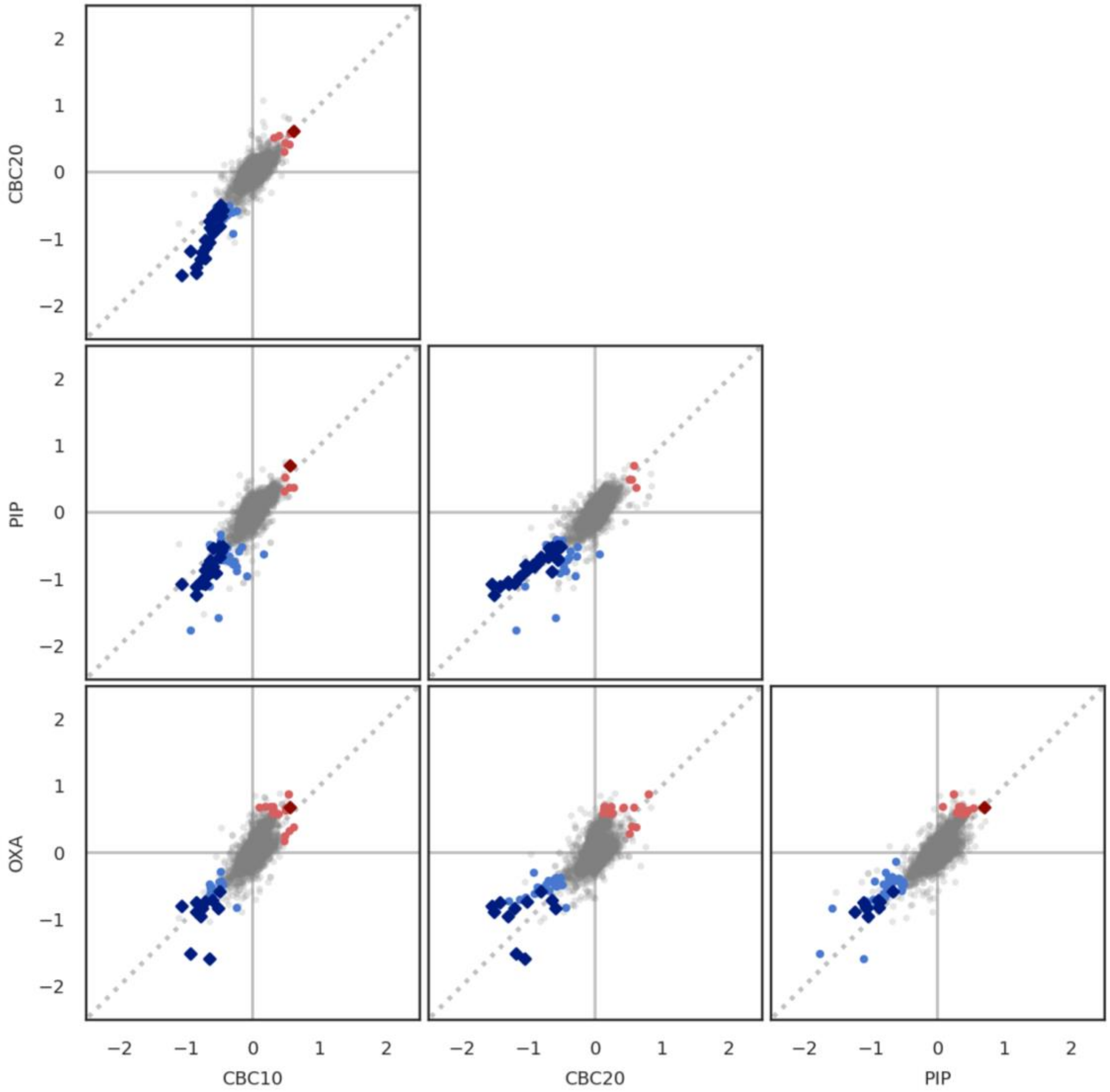

Figure 3.9 | Scatter plots of the relative fitness measurements of the same amino acid changes across different drug selections. Grey dots represent all mutations, bright red dots represent mutants significantly resistance conferring in at least one of the drugs, bright blue dots mutants significantly sensitivity conferring in at least one of the drugs, and dark diamond markers show mutants that are significantly resistance/sensitivity conferring in both drugs.

Most positions in TolC showed optimized efflux activity, with few exhibiting notable fitness deviations (Figure 3.7-3.9). Fifty-one amino acid level replacements in the 428 residues were recorded (Figure 3.10). Eight mutations were common under all selection conditions; all were sensitivity conferring (Figure 3.10A-B).

Consistent with the observation that the structure of TolC is less optimized for carbenicillin efflux than for efflux of the other antibiotics, increasing carbenicillin selection strength from 10 µg/ml to 20 µg/ml resulted in a decrease in the number of resistance-conferring mutations and a simultaneous increase in the number of sensitivity-conferring mutations at the periplasmic region of the protein. Nevertheless, the fitness effects of mutations under different carbenicillin concentrations for selection were highly correlated; of the 27 and 32 mutations recorded in the respective concentrations, 23 were common (Figure 3.10A, Figure 3.9).

The mutations common to all selection conditions were clustered in two regions of the protein: S350A/G, A351C, D356G, D371G, and A375T are all near the periplasmic entry region, while the hydrophobic to polar changes V169T and L175G/T occur near the equatorial domain slightly up the channel (the remaining E29P mutation might destabilize protein folding). Sensitivity-conferring mutations clustered at the periplasmic entrance can disrupt the interactions between the adaptor protein and TolC and prevent the operation of the efflux machinery. Another potential function of these mutations is to enhance the interactions with applied antibiotics and, hence, impede the efflux of antibiotics into the extracellular space (Figure 3.9B, bottom). When we looked at the specifics of how the mutations depended on the selection agents, we found that evolution again exploits the network of local interactions utilized in efflux. Oxacillin, which has low efficacy against *E. coli* because it is highly effluxable by the AcrAB-TolC, leads to the selection of the least number of deviations and potentially the development of further resistance (Figure 3.10A).

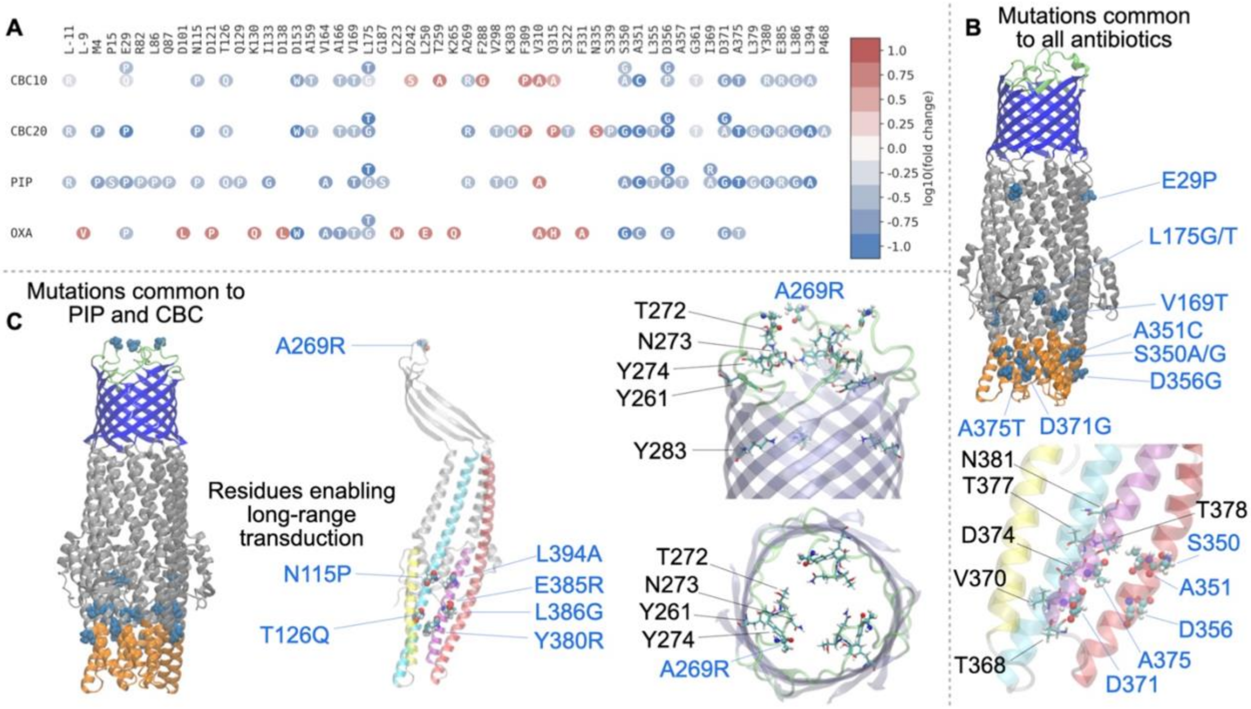

Figure 3.10 | Single mutant library selections reveal the TolC residues critical for efflux activity. *On all structures, sensitivity conferring residues are labeled in blue and those with a high number of antibiotic interactions in SMD simulations in black (Figure 3.4D).* A. Abacus plots summarizing TolC replacements that lead to significant changes in fitness values under selection of carbenicillin (10 µg/ml; CBC10), carbenicillin (20 µg/ml; CBC20), piperacillin (20 µg/ml; PIP), and oxacillin (460 µg/ml; OXA). We used two carbenicillin concentrations to optimize the dynamic range of the fitness values. Excluding synonymous mutations affecting sensitivity, fitness values are represented by a color spectrum from dark blue (more susceptible) to dark red (more resistant). B. Sensitivity conferring residues common to all library selections are shown in space filling. The periplasmic entry region of the single protomer shown below (helices colored as in Figure 3.1C) displays how sensitivity conferring mutations (CPK representation) are in close proximity to residues that display high interactions with the passing drug (licorice representation). C. Mutations shared by carbenicillin, and piperacillin are illustrated in space filling on the whole protein structure (left) and on a protomer in the center. The cluster of residues near the equatorial region enable long-range transduction along the major helices and their disruption via mutations alters the upward motions conferring sensitivity to drugs. On the right, extracellular exit side residues are depicted in both side and top views. The exit is controlled by a set of polar residues with high antibiotic interaction counts (licorice); disruption of the hydrophobic gate by the A269R mutation (CPK) residing on the hydrophobic extracellular loop (green) might disrupt the controlled release of the drugs.

Conversely, the efflux pump had fewer positions that are prone to developing resistance to carbenicillin and piperacillin; most mutations appearing in these backgrounds led to elevated susceptibility to these drugs. In fact, these drugs have seven additional common mutations (Figure 3.10C): those mutations near the equatorial region (N115P and L394A) and those in the region right below (T126Q, Y380R, E385R, L386G) are all in positions where the TolC-carbenicillin/piperacillin interactions are lowest (Figure 3.10A and C) and are in the rigid domains (low RMSFs; Figure 3.9B). We conjecture that these residues occupy important positions that act as the transducers of the intrinsic efflux motions of TolC reflected in the most dominant PCAs. Any mutation that 'softens' this rigidity is expected to alter the efflux mechanism and lead to sensitivity. Common mutations in carbenicillin and piperacillin located at the near equatorial and its right below.

At the final exit region, extensive interactions between the drugs and polar/charged residues Y261, T272, N273, Y274, and Y283 are critical to present the drug to the opening of the portal made up of the flexible hydrophobic patch of residues forming the loop, i.e., G268, A269, A270, G271 (Figure 3.9C, right). The hydrophobic to polar mutation A269R, which confers sensitivity to both carbenicillin and piperacillin, disrupts the hydrophobic balance near the exit region. This may result from redistributing the network of drug-TolC interactions that contribute to the increased amount of work required to expel the charged drug out of this region. We note that this change would be an entropy dominated shift that involves number and distribution of water molecules near the exit side.

3.4 Impact of D371G Mutation on Allosteric Control Mechanisms and Efflux Pump Spanning

Since TolC is optimized for efflux, we tested whether and how these mutations might lead to allosteric effects along with the disrupted local interactions. We selected the D371G mutation that commonly emerged as a sensitivity-conferring mutation in all four of our saturation mutagenesis library selection assays (Figure 3.10A). This is counterintuitive since the replacement of aspartate with glycine, a smaller amino acid with no charge, might be expected to increase the volume available to these negatively charged drugs and make it easier for them to be carried away from the initial entry region. D371 is also the top residue providing the highest correlation coefficient in manipulating both the closed-to-open and open-to-closed conformational change in our PRS analysis (Figure 3.3C).

We conducted 45 SMD simulations on the D371G mutant with carbenicillin and found the energy required for efflux did not change compared to the WT TolC. However, we noted both a minor translation in the curve in the entry region (Figure 3.11A-C) and a substantial reduction in hydrogen bonding partners there (Figure 3.11C).

Drug-free MD simulations with closed form of TolC showed that the substitution D371G eliminates likely dynamic salt bridges with R367 on the neighboring trimeric chain (Figure 3.11D-F).[26,27,29] 100 ns snapshot and 240 ns snapshot were depicted in Figure 3.11E to show the sudden shifts observed in Figure 3.11D, chain B.

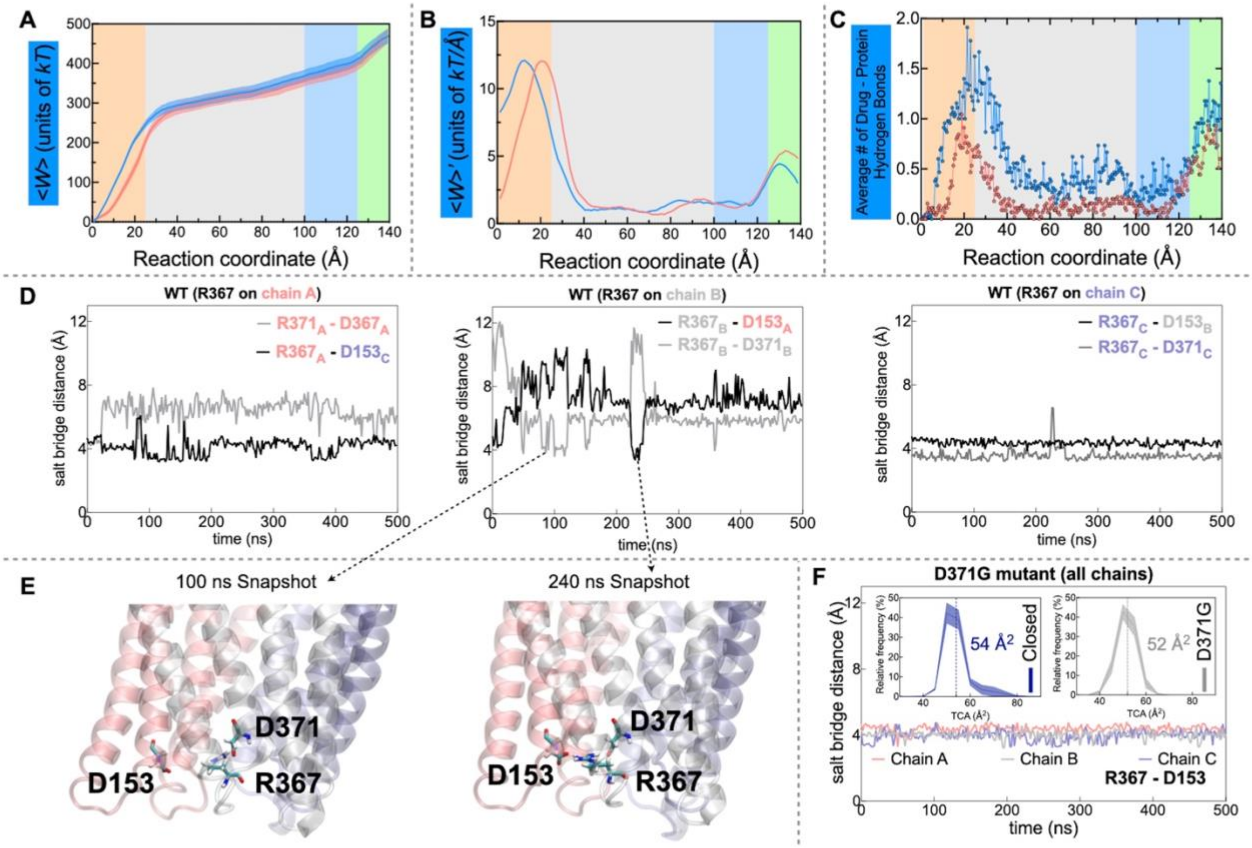

Figure 3.11 | The global and local effects of the D371G mutation on TolC. A-C. Carbenicillin SMD findings comparing wild type and D371G mutant. D. Dynamical shifts in R367 salt bridges on the three chains of wild type TolC in the absence of drugs. Manipulation of R367-D153 salt bridge is necessary to provide flexibility for drug entry and initial efflux (see also Figure 3.6A). R367 has a canonical salt bridge with the D153 on the adjacent chain in the heterotrimer. However, D371 residing on the same chain tends to compete with D153 for this salt bridge. The time evolution of the relevant distances is shown for each chain. E. Possible R367 side chain positions are shown for time points at 100 ns and 240 ns where the interaction swaps between D371 and D153. F. These dynamics are completely lost in the mutant; in the MD simulation for the D371G mutant, the D367-D153 interaction remains constant throughout the 500 ns window of observations. The small shrinkage in the TCA with the introduction of the mutation is shown in the inset (see also Figure 3.6B).

Also, the average TCA of the mutant has a narrower distribution than the wild type of closed form which implies other dynamical interactions are involved in the gating mechanism (Figure 3.11F, inset). The entry point has a triangular set of interactions that includes the salt bridge between R367 on the loop joining H7/H8 and D153 on H4 (Figure 3.6). In addition, the nearby D371 on H8 has the potential to form salt bridges with R367 during the dynamical changes that take place in the background fluctuations of the drug free channel as well as during the passage of drugs. The sensitivity conferring mutations at the periplasmic entry observed in all drugs (Figure 3.9B) have the effect of disrupting these interactions between the effluxed molecule and TolC. Introducing the mutation D371G removed a negatively charged residue that competed with carbenicillin for the interaction with R367 and resulted in a more permanent salt bridge with D153. Recalling that the TCA fluctuated less in this region (Figure 3.1E), we find that this rigidity allowed for a larger volume to accommodate the drug molecule. Paradoxically, this increased the residence time of the drug in the initial trapping region because the dynamical hand-over-hand motions of the drug movement were altered. Moreover, this effect impacted the entire efflux pump (Figure 3.11C) and led to the formation of fewer hydrogen bonds along the whole path. We thus conjecture that the D371G mutation caused an allosteric occlusion effect that changed the efflux pattern of the carbenicillin molecule at the extracellular side.

4. CONCLUSIONS

TolC is an outer membrane protein that plays a crucial role in several cellular functions, including the efflux of antibiotics, bile salts, dyes, and chemicals, as well as the entry of colicin and phages, and haemolysin secretion. The efficiency of TolC in pumping out these substances is highly dependent on the specific molecules involved. While the overall selectivity of the AcrAB-TolC system for drugs can only be partially explained by the processes occurring as the drug traverses TolC, our study delves deeper into the interactions between TolC and drugs, focusing specifically on how TolC contributes to selectivity once the drug has reached its channel.

The closed state conformation is maintained by the network of interactions at the periplasmic side of TolC.[26,27,79,80] The open form is the functioning state of TolC to efflux substrates. Here, we selected charged residues and calculated the TCA during 500 ns MD simulations to show the difference between periplasmic sides at closed and open form proteins. Aperture at the tip of the protein was dilated approximately by 8-fold in the open form simulation. The dilation was decreased for upper tip residues (Figure 3.1E). Also, according to our PRS results, top-ranked residues in closed-to-open and open-to-closed transitions were located at the periplasmic tips of the helices. These results confirmed the importance of periplasmic tip residues (Figure 3.2B-C).

We placed carbenicillin molecule at the three different regions along the closed form of the protein and performed 100 ns simulations to observe its movement along the protein. Carbenicillin molecule encountered a resistance at the periplasmic entrance of the protein (Figure 3.3B, Entry). These results led us to perform SMD with our target antibiotic molecules to observe their key interactions with TolC. Modification of pulling velocity form 0.5 Å ns^{-1} to 5 Å ns^{-1} did not change the work profile of carbenicillin molecule (Figure 3.4). We continued our SMD simulations with 5 Å ns^{-1} where we could get our results faster and increase the number of replicate simulations.

In this study, we focus on three β-lactam antibiotics that are effluxed by TolC at varying rates. SMD simulations support these findings by quantifying the work done during the efflux process and identifying interactions that create barriers along the efflux pathway (Figure 3.4). We tracked the work done as antibiotic molecules move through the protein for 45 simulations. The average work to transport oxacillin is the smallest while carbenicillin is the highest (Figure 3.4A). The rise in hydrogen bonds increased work necessary to efflux carbenicillin (Figure 3.4B). Our "free MD simulations" with the carbenicillin molecule at the three main regions of protein (periplasmic entry; orange, transfer; grey, exit; blue in Figure 1.2B) showed that entry region residues have the highest tendency to make hydrogen bonds with carbenicillin. The transfer region has very few hydrogen bonding residues with carbenicillin. Carbenicillin made some interactions right before leaving the protein.

We measured the average salt bridge donor-acceptor distances during SMD simulations for residues D153, D371, and R367. The negatively charged carbenicillin molecule competes with D153 and D371. Carbenicillin breaks the D153-R367 salt bridge, while the D371-R367 salt bridge remains intact (Figure 3.6A). The D371G mutation reduces the number of negatively charged residues in that region, decreasing the disruption of the D153-R367 salt bridge (Figure 3.6B). Once carbenicillin passes this area, it moves freely for the next 90 Å. Charged and polar residues help by coordinating to push the drug towards the outer part of the channel. Finally, at the exit region, the drug encounters hydrophobic interactions and exits the channel (Supplementary Videos 8 and 9).

The next outcome of our study is related to the DMS of TolC with carbenicillin, piperacillin, and oxacillin antibiotics. We wanted to determine the potential effects of point mutations on fitness of applied antibiotics. We compared mutant residues that conferred significant changes in fitness with the residues that we identified in our MD studies. We used 2.5σ cutoff to detect significant residues (Figure 3.8).

Single residues identified through our experimental screening provide further insights into the efflux mechanisms for each drug molecule. For instance, the movement of piperacillin is primarily impeded in the β barrel embedded in the lipid bilayer near the exit side, whereas the movement of carbenicillin is facilitated by the hydrophobic plug at the entrance and the hydrophobic residues lining the first half of the exit pathway (Figure 3.4C).

Our experimental mutational screen (Figure 3.10A) revealed that mutations in the first ~40 Å region led to increased sensitivity to TolC through several major mechanisms. This is because decreased efflux of antibiotics results in higher effective concentrations of antibiotic molecules inside the cells (Figure 3.10B-C). These mechanisms include direct interference with dynamic TolC-drug interactions during passage, which increases the residence time of the drugs, especially at the entry point. Once an antibiotic enters the channel, the intrinsic movements of TolC assist in transporting the drug through most of the channel (Supplementary Videos 7-9). In particular, mutations in the periplasmic entrance region were common across all tested antibiotics, indicating that these mutations make the efflux of antibiotics more difficult. Although SMD identified residues on H8, DMS revealed mutations primarily on H7, the helix closest to H8. Mutations might indirectly affect antibiotic efflux by disrupting the interactions between residue side chains on the H7/H8 helices.

Our experimental results confirm that TolC is highly optimized for the efflux of oxacillin, a drug very similar to methicillin, which it has replaced in clinical use (Figure 3.10A). Mutations emerging from our screens tend to further increase the resistance of TolC towards this drug. Furthermore, our SMD simulations illustrate the mechanism by which oxacillin is effluxed (Figure 3.4, lower panel). TolC's collective motions are fine-tuned for efflux, even in the absence of drugs (Figure 3.1 and Figure 3.3 and Supplementary Video 3), indicating that any free molecule within this space tends to be carried towards the extracellular side. The rigidity maintained by the equatorial region likely facilitates this efficient efflux mechanism, as key mutations here significantly alter the efflux (Figure 3.10C).

Near the outside, interactions between the drug and polar/charged TolC residues create a final barrier before the drug exits the pump. The exit is guarded by a hydrophobic patch of residues, which may function to gate the entry of pathogens on the extracellular side (Figure 3.10C). Alterations in this region, such as the A269R mutation, disrupt the interactions at the exit; the significantly lowered fitness due to this mutation might be attributed to an uncontrolled opening of the otherwise well-protected exit, making the channel leaky in both directions (Figure 3.10C).

Our mutational scanning experiments and MD simulations demonstrate that TolC is an optimally designed molecular machine for efflux. Our findings suggest that evolutionary selection promotes both local interactions and long-range modifications in the system, which enhance efflux efficiency and maximize bacterial survival (Figure 3.10A). All selected mutations manipulate the network of interactions that temporarily release key salt bridges, moving the drugs along in a hand-over-hand fashion (Supplementary Videos 8 and 9). Notably, these effects are not confined to local changes; shifts in interactions at one end of the channel are communicated to the other end via the intrinsic motions of the pump. This allosteric occlusion effect between the entry and exit regions results from the complex network of interactions within TolC.

Our work paves the way for using standardized pulling simulations (such as SMD) to test the effectiveness of newly designed drugs in efflux pumps. Our findings indicate that drugs designed to manipulate interactions in the entry region of TolC have the best potential to circumvent resistance developed during efflux. This study underscores the importance of understanding the detailed mechanisms of drug efflux through TolC to develop more effective antibiotic therapies and combat bacterial resistance.

5. FUTURE WORK

The three-dimensional structure of the AcrAB-TolC tripartite efflux machinery has already been resolved, providing a broad understanding of its architecture. Building on our current TolC simulations, we propose to conduct MD simulations with the individual components AcrA and AcrB, as well as with combined systems such as TolC-AcrA and AcrA-AcrB. These simulations will help elucidate the interaction dynamics and conformational changes that occur during the efflux process. Furthermore, the SMD simulation studies conducted with the β-lactam antibiotics in this study can be extended to include these new protein complexes, providing insights into the binding and translocation mechanisms of these antibiotics. To broaden the scope of our research, one might expand the variety of β-lactam antibiotics tested, incorporating additional classes such as carbapenem derivatives, including meropenem. These new antibiotic molecules can be subjected to SMD simulations with both the individual target proteins and their complexes. This expanded approach would aim to provide a comprehensive understanding of how different antibiotics interact with the efflux machinery, potentially revealing new paths for overcoming antibiotic resistance.

In addition to the planned MD and SMD simulations, future work might also focus on investigating the interaction dynamics of these protein complexes within more complex bilayer formations. While current simulations have utilized simplified bilayer models, one might also achieve a more physiologically relevant understanding by incorporating complex bilayer compositions that accurately mimic the bacterial inner and outer membranes. These advanced bilayer models might include various lipid species and asymmetrical distributions reflective of natural bacterial membranes. By simulating individual components of the tripartite efflux machinery and complexes such as TolC-AcrA and AcrA-AcrB within these complex bilayers, one might uncover detailed insights into how membrane composition influences protein function and antibiotic translocation. This approach can provide a more comprehensive view of the efflux mechanisms and contribute to the development of strategies to combat antibiotic resistance by targeting the efflux machinery within its native membrane environment.

In this thesis, we investigate the hydrogen bonding of a drug that efflux through the TolC protein using SMD simulations. However, the energy calculations are still insufficient. By employing free energy perturbation (FEP) simulations,[81] it is possible to calculate relative free energies, which can then be compared with experimental energies. This can be done using different conformations from the steered MD simulations, where the drug is located at various positions inside TolC. Apart from the FEP simulations, the effect of different mutations can be scrutinized using the Mutation-Minimization (MuMi)[82] scheme, where each single mutation is introduced and then minimized in water. Again, starting with different conformations where the drug is located at different parts of TolC, the effect of mutation on hydrogen bonds might be explained in more detail.

Furthermore, the analysis of SMD trajectories can be done using dynamic community analysis,[83,84] where one may assess changes in different groups (communities) of residues that are important for protein function. By focusing on the efflux of a drug molecule, the time evolution of communities may shed light on the mechanism of the TolC protein. Combined with MuMi, these community analyses may explain the local and global effects of mutations for each drug molecule.

Since TolC is a part of the drug efflux machinery, performing coarse-grained simulations with the Martini force field[85] and reverse mapping to identify conformational changes can be an option to understand the overall dynamics of the AcrAB-TolC machinery.

TolC efflux rate becomes inadequate when the antibiotic concentration reaches the upper limit, causing the antibiotic to accumulate in the bacteria and kill them. We illustrated the optimal concentrations for carbenicillin, piperacillin, and oxacillin to kill *tolC*-containing strains (Figure 2.1B-D and Table 2.1). MD simulations cannot provide the concentration information of antibiotic molecules within TolC. However, we can perform classical MD simulations with TolC containing multiple antibiotic molecules in different regions of the protein for more comprehensive analysis.

Another approach to understand the antibiotic efflux involves conducting SMD simulations with multiple antibiotic molecules. Antibiotics can be strategically positioned at the periplasmic side and begin to pull one of them. After a certain point, we can start pulling another antibiotic from the queue. By observing the effects as each antibiotic is pulled from the queue, we can gain insights into the collective impact of multiple antibiotic molecules on the protein.

APPENDIX A

Chemicals and Bacterial Strains

Amicase (82514, Sigma)
BW25113 *E. coli* strain (CGSC No.: 7636)
Carbenicillin (C3416, Sigma-Aldrich)
ΔtolC732::kan E. coli strain (CGSC No.: 11430)
Glucose (50-99-7, Fisher Scientific)
Kanamycin (60616, Sigma-Aldrich)
M9 minimal medium (248510, Difco)
NEBuilder HiFi DNA Assembly Kit (E5520, New England Biolabs)
Oxacillin (NDC25021-162-24 Sagent Pharmaceuticals)
Piperacillin (P8396, Sigma-Aldrich)
pSF-Oxb14 plasmid Oxford Genetics (OGS557, Sigma)

APPENDIX B

Supplementary Videos

The coloring scheme for protein maintained throughout the manuscript is also valid for Supplementary Videos. Residues that formed two or more hydrogen bonds for each antibiotic molecule are highlighted as dynamic bonds. Positively charged residues are red, polar residues are violet, and hydrophobic residues are cyan-colored. In addition to these hydrogen bonding residues, R367 is highlighted as red and D371 is highlighted as blue.

Supplementary Video 1 | PC1 obtained from the 460-500 ns portion of the closed trajectory.

Supplementary Video 2 | PC2 obtained from the 460-500 ns portion of the closed trajectory.

Supplementary Video 3 | PC3 obtained from the 460-500 ns portion of the closed trajectory.

Supplementary Video 4 | PC1 obtained from the 460-500 ns portion of the open form trajectory.

Supplementary Video 5 | PC2 obtained from the 460-500 ns portion of the open form trajectory.

Supplementary Video 6 | PC3 obtained from the 460-500 ns portion of the open form trajectory.

Supplementary Video 7 | Sample SMD trajectory displaying the interactions of carbenicillin with the high contact residues in TolC.

Supplementary Video 8 | Sample SMD trajectory displaying the interactions of piperacillin with the high contact residues in TolC.

Supplementary Video 9 | Sample SMD trajectory displaying the interactions of oxacillin with the high contact residues in TolC.

REFERENCES

1. Murray, C. J. L. *et al.* Global burden of bacterial antimicrobial resistance in 2019: a systematic analysis. *The Lancet* **399**, 629–655 (2022).

2. Breijyeh, Z., Jubeh, B. & Karaman, R. Resistance of Gram-Negative Bacteria to Current Antibacterial Agents and Approaches to Resolve It. *Molecules* **25**, 1340 (2020).

3. Lee, J.-H. Perspectives towards antibiotic resistance: from molecules to population. *J. Microbiol.* **57**, 181–184 (2019).

4. Fernández, L., Breidenstein, E. B. M. & Hancock, R. E. W. Creeping baselines and adaptive resistance to antibiotics. *Drug Resist. Updat.* **14**, 1–21 (2011).

5. Christaki, E., Marcou, M. & Tofarides, A. Antimicrobial Resistance in Bacteria: Mechanisms, Evolution, and Persistence. *J. Mol. Evol.* **88**, 26–40 (2020).

6. Holmes, A. H. *et al.* Understanding the mechanisms and drivers of antimicrobial resistance. *The Lancet* **387**, 176–187 (2016).

7. Munita, J. M. & Arias, C. A. Mechanisms of Antibiotic Resistance. *Microbiol. Spectr.* **4**, 4.2.15 (2016).

8. Blair, J. M., Richmond, G. E. & Piddock, L. J. Multidrug efflux pumps in Gram-negative bacteria and their role in antibiotic resistance. *Future Microbiol.* **9**, 1165–1177 (2014).

9. Kumar, A. & Schweizer, H. Bacterial resistance to antibiotics: Active efflux and reduced uptake. *Adv. Drug Deliv. Rev.* **57**, 1486–1513 (2005).

10. Poole, K. Efflux-mediated multiresistance in Gram-negative bacteria. *Clin. Microbiol. Infect.* **10**, 12–26 (2004).

11. Paulsen, I. T., Park, J. H., Choi, P. S. & Saier, M. H. A family of Gram-negative bacterial outer membrane factors that function in the export of proteins, carbohydrates, drugs and heavy metals from Gram-negative bacteria. *FEMS Microbiol. Lett.* **156**, 1–8 (2006).

12. Nikaido, H. Multidrug efflux pumps of gram-negative bacteria. *J. Bacteriol.* **178**, 5853–5859 (1996).

13. Nikaido, H. Multidrug Resistance in Bacteria. *Annu. Rev. Biochem.* **78**, 119–146 (2009).

14. Levy, S. B. & Marshall, B. Antibacterial resistance worldwide: causes, challenges and responses. *Nat. Med.* **10**, S122–S129 (2004).

15. Poole, K. Outer Membranes and Efflux: The Path to Multidrug Resistance in Gram- Negative Bacteria. *Curr. Pharm. Biotechnol.* **3**, 77–98 (2002).

16. Nikaido, H. Structure and Mechanism of RND-Type Multidrug Efflux Pumps. in *Advances in Enzymology - and Related Areas of Molecular Biology* (ed. Toone, E. J.) vol. 77 1–60 (Wiley, 2011).

17. Fralick, J. A. Evidence that TolC is required for functioning of the Mar/AcrAB efflux pump of Escherichia coli. *J. Bacteriol.* **178**, 5803–5805 (1996).

18. Piddock, L. J. V. Multidrug-resistance efflux pumps ? not just for resistance. *Nat. Rev. Microbiol.* **4**, 629–636 (2006).

19. Darzynkiewicz, Z. M. *et al.* Identification of Binding Sites for Efflux Pump Inhibitors of the AcrAB-TolC Component AcrA. *Biophys. J.* **116**, 648–658 (2019).

20. De Zwaig, R. N. & Luria, S. E. Genetics and Physiology of Colicin-tolerant Mutants of *Escherichia coli*. *J. Bacteriol.* **94**, 1112–1123 (1967).

21. Davies, J. K. & Reeves, P. Genetics of resistance to colicins in Escherichia coli K-12: cross-resistance among colicins of group B. *J. Bacteriol.* **123**, 96–101 (1975).

22. German, G. J. & Misra, R. The TolC protein of Escherichia coli serves as a cell-surface receptor for the newly characterized TLS bacteriophage 1 1Edited by B. Holland. *J. Mol. Biol.* **308**, 579–585 (2001).

23. Ayhan, D. H. *et al.* Sequence-Specific Targeting of Bacterial Resistance Genes Increases Antibiotic Efficacy. *PLOS Biol.* **14**, e1002552 (2016).

24. Puchta, O. *et al.* Network of epistatic interactions within a yeast snoRNA. *Science* **352**, 840–844 (2016).

25. Koronakis, V., Sharff, A., Koronakis, E., Luisi, B. & Hughes, C. Crystal structure of the bacterial membrane protein TolC central to multidrug efflux and protein export. *Nature* **405**, 914–919 (2000).

26. Bavro, V. N. *et al.* Assembly and Channel Opening in a Bacterial Drug Efflux Machine. *Mol. Cell* **30**, 114–121 (2008).

27. Wang, Z. *et al.* An allosteric transport mechanism for the AcrAB-TolC multidrug efflux pump. *eLife* **6**, e24905 (2017).

28. Pei, X.-Y. *et al.* Structures of sequential open states in a symmetrical opening transition of the TolC exit duct. *Proc. Natl. Acad. Sci.* **108**, 2112–2117 (2011).

29. Marshall, R. L. & Bavro, V. N. Mutations in the TolC Periplasmic Domain Affect Substrate Specificity of the AcrAB-TolC Pump. *Front. Mol. Biosci.* **7**, 166 (2020).

30. Atilgan, A. R. *et al.* Anisotropy of Fluctuation Dynamics of Proteins with an Elastic Network Model. *Biophys. J.* **80**, 505–515 (2001).

31. Phan, G. *et al.* Structural and Dynamical Insights into the Opening Mechanism of P. aeruginosa OprM Channel. *Structure* **18**, 507–517 (2010).

32. Newman, K. E. & Khalid, S. Conformational dynamics and putative substrate extrusion pathways of the N-glycosylated outer membrane factor CmeC from Campylobacter jejuni. *PLOS Comput. Biol.* **19**, e1010841 (2023).

33. Izrailev, S., Stepaniants, S., Balsera, M., Oono, Y. & Schulten, K. Molecular dynamics study of unbinding of the avidin-biotin complex. *Biophys. J.* **72**, 1568–1581 (1997).

34. Jolliffe, I. Principal Component Analysis. in *Encyclopedia of Statistics in Behavioral Science* (eds. Everitt, B. S. & Howell, D. C.) (Wiley, 2005). doi:10.1002/0470013192.bsa501.

35. Lange, O. F. *et al.* Recognition Dynamics Up to Microseconds Revealed from an RDC-Derived Ubiquitin Ensemble in Solution. *Science* **320**, 1471–1475 (2008).

36. Atilgan, C. & Atilgan, A. R. Perturbation-Response Scanning Reveals Ligand Entry-Exit Mechanisms of Ferric Binding Protein. *PLoS Comput. Biol.* **5**, e1000544 (2009).

37. Atilgan, C., Gerek, Z. N., Ozkan, S. B. & Atilgan, A. R. Manipulation of Conformational Change in Proteins by Single-Residue Perturbations. *Biophys. J.* **99**, 933–943 (2010).

38. Penkler, D. L., Atilgan, C. & Tastan Bishop, Ö. Allosteric Modulation of Human Hsp90α Conformational Dynamics. *J. Chem. Inf. Model.* **58**, 383–404 (2018).

39. Ross, C. J., Atilgan, A. R., Tastan Bishop, Ö. & Atilgan, C. Unraveling the Motions behind Enterovirus 71 Uncoating. *Biophys. J.* **114**, 822–838 (2018).

40. Leach, A. R. *Molecular Modelling: Principles and Applications*. (Prentice Hall, Harlow, England ; New York, 2001).

41. Schrödinger, LLC. The PyMOL Molecular Graphics System, Version 1.8. (2015).

42. Lomize, M. A., Pogozheva, I. D., Joo, H., Mosberg, H. I. & Lomize, A. L. OPM database and PPM web server: resources for positioning of proteins in membranes. *Nucleic Acids Res.* **40**, D370–D376 (2012).

43. Lomize, A. L., Todd, S. C. & Pogozheva, I. D. Spatial arrangement of proteins in planar and curved membranes by PPM 3.0. *Protein Sci.* **31**, 209–220 (2022).

44. Jo, S., Kim, T. & Im, W. Automated Builder and Database of Protein/Membrane Complexes for Molecular Dynamics Simulations. *PLoS ONE* **2**, e880 (2007).

45. Lee, J. *et al.* CHARMM-GUI Input Generator for NAMD, GROMACS, AMBER, OpenMM, and CHARMM/OpenMM Simulations Using the CHARMM36 Additive Force Field. *J. Chem. Theory Comput.* **12**, 405–413 (2016).

46. Jo, S., Kim, T., Iyer, V. G. & Im, W. CHARMM-GUI: A web-based graphical user interface for CHARMM. *J. Comput. Chem.* **29**, 1859–1865 (2008).

47. Best, R. B. *et al.* Optimization of the Additive CHARMM All-Atom Protein Force Field Targeting Improved Sampling of the Backbone ϕ, ψ and Side-Chain χ_1 and χ_2 Dihedral Angles. *J. Chem. Theory Comput.* **8**, 3257–3273 (2012).

48. Jorgensen, W. L., Chandrasekhar, J., Madura, J. D., Impey, R. W. & Klein, M. L. Comparison of simple potential functions for simulating liquid water. *J. Chem. Phys.* **79**, 926–935 (1983).

49. Phillips, J. C. *et al.* Scalable molecular dynamics with NAMD. *J. Comput. Chem.* **26**, 1781–1802 (2005).

50. Phillips, J. C. *et al.* Scalable molecular dynamics on CPU and GPU architectures with NAMD. *J. Chem. Phys.* **153**, 044130 (2020).

51. Essmann, U. *et al.* A smooth particle mesh Ewald method. *J. Chem. Phys.* **103**, (1995).

52. Andersen, H. C. Rattle: A “velocity” version of the shake algorithm for molecular dynamics calculations. *J. Comput. Phys.* **52**, 24–34 (1983).

53. Bakan, A. & Bahar, I. The intrinsic dynamics of enzymes plays a dominant role in determining the structural changes induced upon inhibitor binding. *Proc. Natl. Acad. Sci.* **106**, 14349–14354 (2009).

54. Bakan, A., Meireles, L. M. & Bahar, I. ProDy: Protein Dynamics Inferred from Theory and Experiments. *Bioinformatics* **27**, 1575–1577 (2011).

55. Bakan, A. *et al. Evol* and *ProDy* for bridging protein sequence evolution and structural dynamics. *Bioinformatics* **30**, 2681–2683 (2014).

56. Zhang, S. *et al. ProDy* 2.0: increased scale and scope after 10 years of protein dynamics modelling with Python. *Bioinformatics* **37**, 3657–3659 (2021).

57. Bahar, I., Lezon, T. R., Bakan, A. & Shrivastava, I. H. Normal Mode Analysis of Biomolecular Structures: Functional Mechanisms of Membrane Proteins. *Chem. Rev.* **110**, 1463–1497 (2010).

58. Henzler-Wildman, K. A. *et al.* Intrinsic motions along an enzymatic reaction trajectory. *Nature* **450**, 838–844 (2007).

59. Henzler-Wildman, K. A. *et al.* A hierarchy of timescales in protein dynamics is linked to enzyme catalysis. *Nature* **450**, 913–916 (2007).

60. Brooks, B. R., Janežič, D. & Karplus, M. Harmonic analysis of large systems. I. Methodology. *J. Comput. Chem.* **16**, 1522–1542 (1995).

61. Case, D. A. Normal mode analysis of protein dynamics. *Curr. Opin. Struct. Biol.* **4**, 285–290 (1994).

62. Skjaerven, L., Martinez, A. & Reuter, N. Principal component and normal mode analysis of proteins; a quantitative comparison using the GroEL subunit. *Proteins Struct. Funct. Bioinforma.* **79**, 232–243 (2011).

63. Bauer, J. A., Pavlović, J. & Bauerová-Hlinková, V. Normal Mode Analysis as a Routine Part of a Structural Investigation. *Molecules* **24**, 3293 (2019).

64. Atilgan, C., Okan, O. B. & Atilgan, A. R. Network-Based Models as Tools Hinting at Nonevident Protein Functionality. *Annu. Rev. Biophys.* **41**, 205–225 (2012).

65. Okan, O. B., Atilgan, A. R. & Atilgan, C. Nanosecond Motions in Proteins Impose Bounds on the Timescale Distributions of Local Dynamics. *Biophys. J.* **97**, 2080–2088 (2009).

66. Penkler, D., Sensoy, Ö., Atilgan, C. & Tastan Bishop, Ö. Perturbation–Response Scanning Reveals Key Residues for Allosteric Control in Hsp70. *J. Chem. Inf. Model.* **57**, 1359–1374 (2017).

67. Jalalypour, F., Sensoy, O. & Atilgan, C. Perturb–Scan–Pull: A Novel Method Facilitating Conformational Transitions in Proteins. *J. Chem. Theory Comput.* **16**, 3825–3841 (2020).

68. Binnig, G., Quate, C. F. & Gerber, Ch. Atomic Force Microscope. *Phys. Rev. Lett.* **56**, 930–933 (1986).

69. Jarzynski, C. Nonequilibrium Equality for Free Energy Differences. *Phys. Rev. Lett.* **78**, 2690–2693 (1997).

70. Liu, Y. *et al.* CB-Dock2: improved protein-ligand blind docking by integrating cavity detection, docking and homologous template fitting. *Nucleic Acids Res.* **50**, (2022).

71. Brooks, B. R. *et al.* CHARMM: The biomolecular simulation program. *J. Comput. Chem.* **30**, (2009).

72. Kim, S. *et al.* CHARMM-GUI ligand reader and modeler for CHARMM force field generation of small molecules. *J. Comput. Chem.* **38**, (2017).

73. Nategholeslam, M., Gray, C. G. & Tomberli, B. Stiff Spring Approximation Revisited: Inertial Effects in Nonequilibrium Trajectories. *J. Phys. Chem. B* **121**, 391–403 (2017).

74. Baba, T. *et al.* Construction of *Escherichia coli* K-12 in-frame, single-gene knockout mutants: the Keio collection. *Mol. Syst. Biol.* **2**, 2006.0008 (2006).

75. Tamer, Y. T. *et al.* The Antibiotic Efflux Protein TolC Is a Highly Evolvable Target under Colicin E1 or TLS Phage Selection. *Mol. Biol. Evol.* **38**, 4493–4504 (2021).

76. Datsenko, K. A. & Wanner, B. L. One-step inactivation of chromosomal genes in *Escherichia coli* K-12 using PCR products. *Proc. Natl. Acad. Sci.* **97**, 6640–6645 (2000).

77. Weng, J. & Wang, W. Structural Features and Energetics of the Periplasmic Entrance Opening of the Outer Membrane Channel TolC Revealed by Molecular Dynamics Simulation and Markov State Model Analysis. *J. Chem. Inf. Model.* **59**, 2359–2366 (2019).

78. Vaccaro, L., Scott, K. A. & Sansom, M. S. P. Gating at Both Ends and Breathing in the Middle: Conformational Dynamics of TolC. *Biophys. J.* **95**, 5681–5691 (2008).

79. Andersen, C. *et al.* Transition to the open state of the TolC periplasmic tunnel entrance. *Proc. Natl. Acad. Sci.* **99**, 11103–11108 (2002).

80. Augustus, A. M., Celaya, T., Husain, F., Humbard, M. & Misra, R. Antibiotic-Sensitive TolC Mutants and Their Suppressors. *J. Bacteriol.* **186**, 1851–1860 (2004).

81. Guclu, T. F., Kocatug, N., Atilgan, A. R. & Atilgan, C. N-Terminus of the Third PDZ Domain of PSD-95 Orchestrates Allosteric Communication for Selective Ligand Binding. *J. Chem. Inf. Model.* **61**, 347–357 (2021).

82. Ozbaykal, G., Atilgan, A. R. & Atilgan, C. In silico mutational studies of Hsp70 disclose sites with distinct functional attributes. *Proteins Struct. Funct. Bioinforma.* **83**, 2077–2090 (2015).

83. Guclu, T. F., Atilgan, A. R. & Atilgan, C. Dynamic Community Composition Unravels Allosteric Communication in PDZ3. *J. Phys. Chem. B* **125**, 2266–2276 (2021).

84. Cetin, E. *et al.* Kinetic Barrier to Enzyme Inhibition Is Manipulated by Dynamical Local Interactions in E. coli DHFR. *J. Chem. Inf. Model.* **63**, 4839–4849 (2023).

85. Marrink, S. J., Risselada, H. J., Yefimov, S., Tieleman, D. P. & De Vries, A. H. The MARTINI Force Field: Coarse Grained Model for Biomolecular Simulations. *J. Phys. Chem. B* **111**, 7812–7824 (2007).